CFD study of wave interaction with single and two tandem circular cylinders

Zhenghao Liu, Weiwen Zhao, Decheng Wan [*]

Computational Marine Hydrodynamics Lab (CMHL), School of Naval Architecture, Ocean and Civil Engineering, Shanghai Jiao Tong University, Shanghai, 200240, China

ARTICLE INFO

ABSTRACT

Wave-structure interaction is a key consideration for the safe design of offshore structures. This work investigates the non-linear wave interactions with a single cylinder and two tandem cylinders using a numerical wave tank. The numerical simulations are carried out by the in-house CFD solver naoe-FOAM-SJTU, which is developed on the open-source platform OpenFOAM. The numerical simulation is first validated by comparing numerical results and experimental data for regular wave interaction with a single cylinder. Wave interaction with tandem cylinders is then investigated for different center-to-center distances between the cylinders. The surface elevation around the cylinder is probed by a series of wave probes and analyzed using the Fast Fourier analysis. The response amplitude operates of surface elevation for single cylinder case agrees well with experimental data. The wave scattering around the cylinder is qualitatively compared with experimental observation and discussed in detail. The wave scattering fields and wave forces are systematically analyzed. Then the interaction between wave and two tandem cylinders is investigated. The distance between the cylinders highly influences the free surface elevation and wave forces experienced by the tandem cylinders. The local surface elevation and the scattered wave field around the cylinders are also discussed.

1. Introduction

Offshore structures such as Spars, semi-submersibles and tension leg platforms (TLP) have been widely applied in ocean engineering. Such platforms usually have large vertical supporting columns, which may cause significant free surface magnification near the columns in wave conditions. Two effects generally cause the magnification: wave enhancement due to fluid interaction among the platform's columns and wave run-up on columns, which are essential for airgap design for a platform (Shan et al., 2011). In severe ocean environments, wave run-up on the large columns of the offshore structures can be relatively high and even causes green water on deck. Thus, understanding the interaction between waves and large columns is vital for the airgap design of a platform. Numerous researchers have done experimental, theoretical, and numerical studies on wave-structure interactions, such as harmonic wave loads, wave run-up on both fixed and floating offshore structures.

A physical experiment is one of the most common approaches to study wave-structure interaction. Various experimental investigations of wave run-up on vertical cylinders have previously been performed. Galvin and Hallermeier (1972) experimentally studied the distribution

of free surface around a cylindrical column by mounting a series of wave gauges near the column. The effects of wave period, wave height, and cylinder cross-section on free surface distribution around the cylinder were discussed. It was found that the wave pattern around the cylinder depends more on wave height and cylinder cross-section than on wave period. Chakrabarti and Tam (1975) conducted model tests to investigate the regular waves onto a large-scale cylinder. Their work was focused on the relationship between the wave run-up and the incident wave height. They found that when the wave amplitudes become large compared to the water depth, second-order effects are expected to be significant. In this case, the non-linear terms in the Navier-Stokes equation are no longer negligible and should be included in the analysis. Kriebel (1992) found that the run-up may reach an elevation of more than twice the incident wave crest amplitude for steep waves. Contento et al. (1998) investigated the local pressure and wave loads on the cylinder and the wave pattern around the cylinder under regular waves. Martin et al. (2001) experimentally studied the run-up on slender columns in steep, deep water waves. All the theories, including linear diffraction, a superposition method, velocity stagnation head, and a related semi-empirical method in their work, underpredicted the wave

---

* Corresponding author.
  E-mail address: dcwan@sjtu.edu.cn (D. Wan).
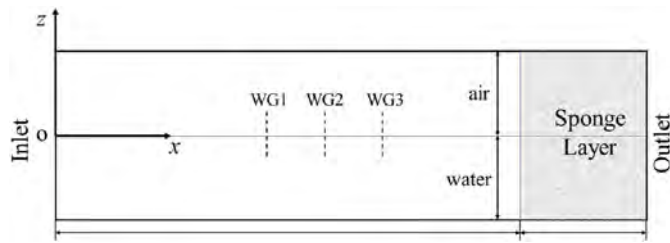
Fig. 1. Schematic of the computational domain of the numerical wave tank.
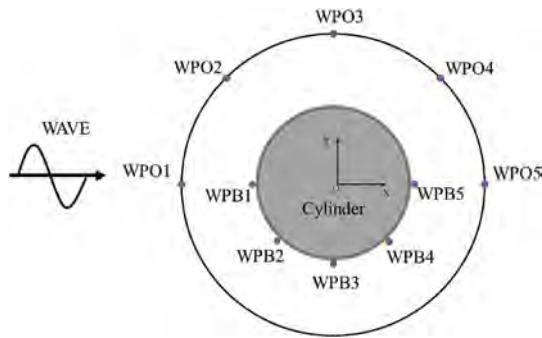
Fig. 2. The layout of wave probes.

Table 1
The location of wave probes.

Inner circle	x (m)	y (m)	Outer circle	x (m)	y (m)
WPB1	−8.2063	0.0000	WPO1	−16.0000	0.0000
WPB2	−5.8027	−5.8027	WPO2	−11.3137	−11.3137
WPB3	0.0000	−8.2063	WPO3	0.0000	16.0000
WPB4	5.8027	−5.8027	WPO4	11.3137	11.3137
WPB5	8.2063	0.0000	WPO5	16.0000	0.0000
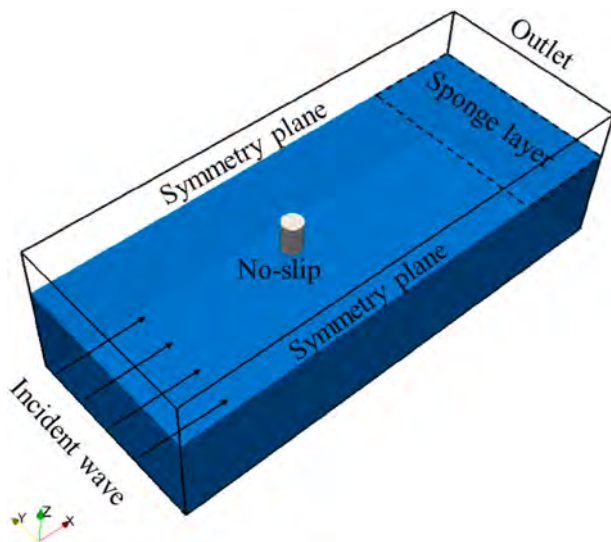
Fig. 3. Computational domain.

run-up value by a significant margin. The effects of wave steepness and the scattering parameter have been investigated by Morris-Thomas et al. (2002). They used a discrete Fourier transform method to extract the zero-, first- and second-harmonic components of wave run-up. The extracted harmonic components were compared with the results predicted by the potential flow theory. It was shown that the modulus of the

first-harmonic component could be well predicted by linear diffraction theory, while the zero-harmonic and the second-harmonic components were not well captured. A comparative study of airgap and run-up based on potential theories was reported by Nielsen (2003). He found that the linear methods can only predict reasonable crest elevations at very low wave steepness, and the second-order method can generally give better results than the linear methods. The effect of cross-sectional shape on the wave run-up surrounding the cylinders was also investigated. Compared with a circular cylinder, stronger non-linear interaction can be found for a circular-like cylinder. Contento et al. (2004) conducted experimental tests to study "near trapping" and the second-order near trapping for an array of circular cylinders. They found that first-order near trapping occurs at the incident wave frequency, whereas second-order near-trapping is a double frequency phenomenon. Systematic model tests were conducted in Shanghai Jiaotong University to investigate the effect of aspect ratio, cross-sectional shape, wave parameters, and current on wave run-up phenomenon in 2010. As part of this work, Shan et al. (2011) reported the relationship between airgap distributions and wave parameters and discussed wave run-up characteristics along with square columns for both fixed and floating models. They found that the motion of semi-submersible will affect wave run-up, airgap distributions, and wave patterns. The degree largely depends on the relationship between the wave period and the natural period of the platform. Ramirez et al. (2013) conducted a large-scale experimental study investigating wave run-up on a circular cylinder in irregular waves. They considered that the waveform should be considered to predict the wave run-up in extreme wave conditions. To investigate wave run-up, the ITTC committee organized several studies, including experimental and numerical researches, in 2013. The results of a series of model tests for a truncated circular column in regular waves performed at MARINTEK and MOERI (Kristiansen et al., 2004) are used in the ITTC benchmark study. The time histories and harmonic components of free-surface elevations and wave forces under different steepnesses and periods were provided.

Besides experimental research on wave run-up, theoretical methods have been widely used to predict wave run-up and wave loading on offshore structures (Cao et al., 2017). Theoretical methods were based initially on the Morison equation or potential flow theory. In the early days, the approximate results of wave run-up on a single-cylinder were acquired according to first and second-order potential flow theory (Havelock, 1940). Trulsen and Teigen (2002) developed a fully non-linear potential flow model to investigate the interaction between waves and a fixed vertical truncated cylinder and compared the predicted linear and second-order results with experimental data. They found that their numerical method cannot agree well with the experimental results. Even for small Keulegan-Carpenter (KC) numbers, the manifestation of viscosity may affect the wave elevation measurements, which the potential flow calculations could not capture. Similar researches can be found in Teigen and Niedzwecki (2003). Morris-Thomas and Thiagarajan (2004) adopted the linear diffraction theory and the commercial software WAMIT to predict the wave run-up around a vertical cylinder. They suggested that linear diffraction theory is insufficient for wave run-up estimation. The second-order harmonic components predicted by WAMIT show relatively accurate estimation of wave run-up when the scattering parameter is small. Gentaz et al. (2004) applied Spectral Wave Explicit Navier-Stokes Equations (SWENSE) approach to simulate a vertical cylinder in non-linear waves. Matsumoto et al. (2013) studied the wave run-up and airgap for a large semi-submersible unit in both fixed and moored configurations. The numerical model WAMIT based on second-order diffraction theory and viscous code ComFLOW were adopted in their work. For higher steepness cases (0.0486–0.0548) in their study, ComFLOW predicted precisely the same values of free surface elevation compared to the experimental data, whereas WAMIT presented some discrepancies. This indicates that higher-order components may have a significant influence on wave run-up during the interaction between wave and the platform
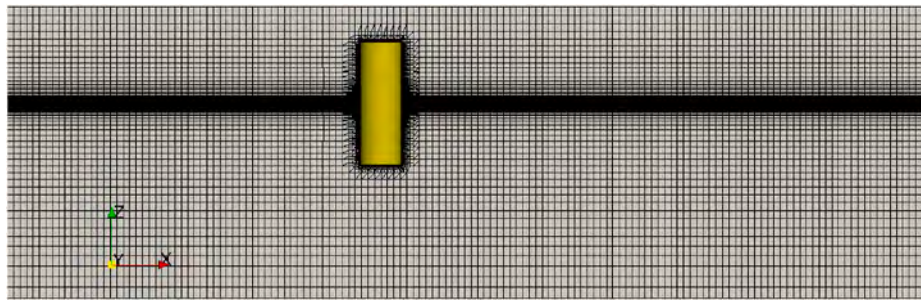
Fig. 4. Mesh of the computational domain.

Table 2
Test conditions.

	T (s)	H/L	L (m)	H (m)	D/L	KC
case 1	7	1/30	76.44	2.548	0.209	0.500
case 2	7	1/16	76.44	4.777	0.209	0.938
case 3	7	1/10	76.44	7.644	0.209	1.501
case 4	9	1/30	126.36	4.212	0.127	0.827
case 5	9	1/16	126.36	7.898	0.127	1.551
case 6	9	1/10	126.36	12.636	0.127	2.481
case 7	15	1/30	351.00	11.700	0.046	2.297
case 8	15	1/16	351.00	21.938	0.046	4.307
case 9	15	1/10	351.00	35.100	0.046	6.892

for those cases. Cao et al. (2017) proposed a new prediction method using two non-dimensionalized parameters: one is the ratio of the run-up to the total head of incident wave $R/(\eta_{max} + u_{max}^2/2g)$, the other is a fitted functional form for the dependence on the scattering parameter.

Generally, theoretical methods based on potential theory could not accurately predict wave run-up on cylinders for steep waves or complex structures. Besides, the limitation of these methods is that they have to be modified for different geometries and different wave conditions (Sun

et al., 2016; Cao and Wan, 2017). With the rapid development of computer technology during the last several decades, the computational fluid dynamics (CFD) method based on Navier-Stokes equations has been widely applied in ocean engineering. Previous numerical simulations based on CFD have also been performed on wave run-up problems. Lee et al. (2007) investigated the wave run-up on fixed single and double cylinders by the newly developed 3D volume of fluid (VOF) method based on two-step projection. Their method can provide some satisfactory results compared to the data provided by Sanada (1998). Danmeier et al. (2008) used the software ComFLOW to simulate the wave run-up around a semi-submersible platform. Nam et al. (2012) developed a two-phase Navier-Stokes solver based on the collocated finite volume method (FVM) with the VOF approach. 3D diffraction problems for a bottom-mounted cylinder were simulated. The calculated wave-induced loads and run-ups agreed well with potential flow solutions. Yoon et al. (2016) assessed the capabilities of two versions of CFDShip-Iowa V4.5 and V6.2 to simulate wave run-up for single/multiple surface-piercing cylinders in regular waves.

More recently, the open-source platform OpenFOAM has been widely used to deal with wave-structure interaction problems. Chen et al. (2014) applied OpenFOAM to simulate regular and irregular waves
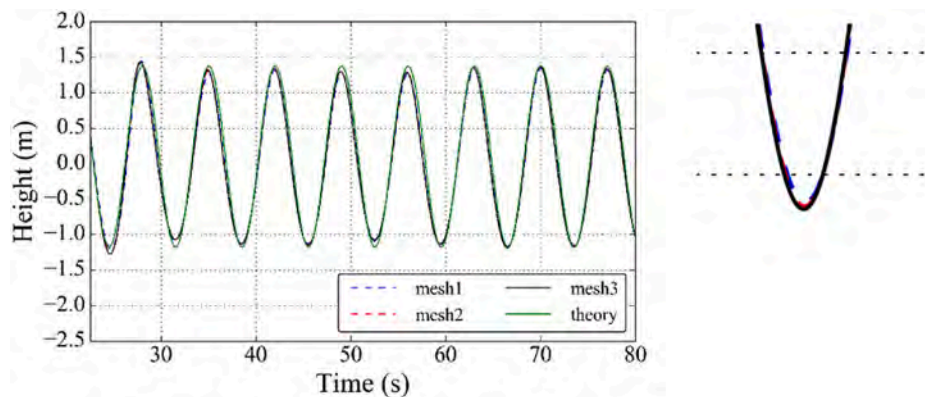
Fig. 5. Time histories of surface elevations without cylinder based on different meshes.

Table 3
Grid convergence study for case 1.

Grid	ID	Grid Size	RAO of WPB1	Error of RAO	$F_x^{(1)}/\rho g A r^2$	Error of F_x
EFD			1.586		5.583	
fine	S1	4.72M	1.552	−2.14%	5.327	−4.58%
medium	S2	2.51M	1.533	−3.34%	5.243	−6.08%
coarse	S3	1.41M	1.412	−10.97%	4.931	−11.57%
R_G			0.157		0.269	
P			5.366		3.79	
GCI_{12}			0.28%		0.69%	
GCI_{23}			1.76%		2.53%	
Convergence type			Monotonic		Monotonic	
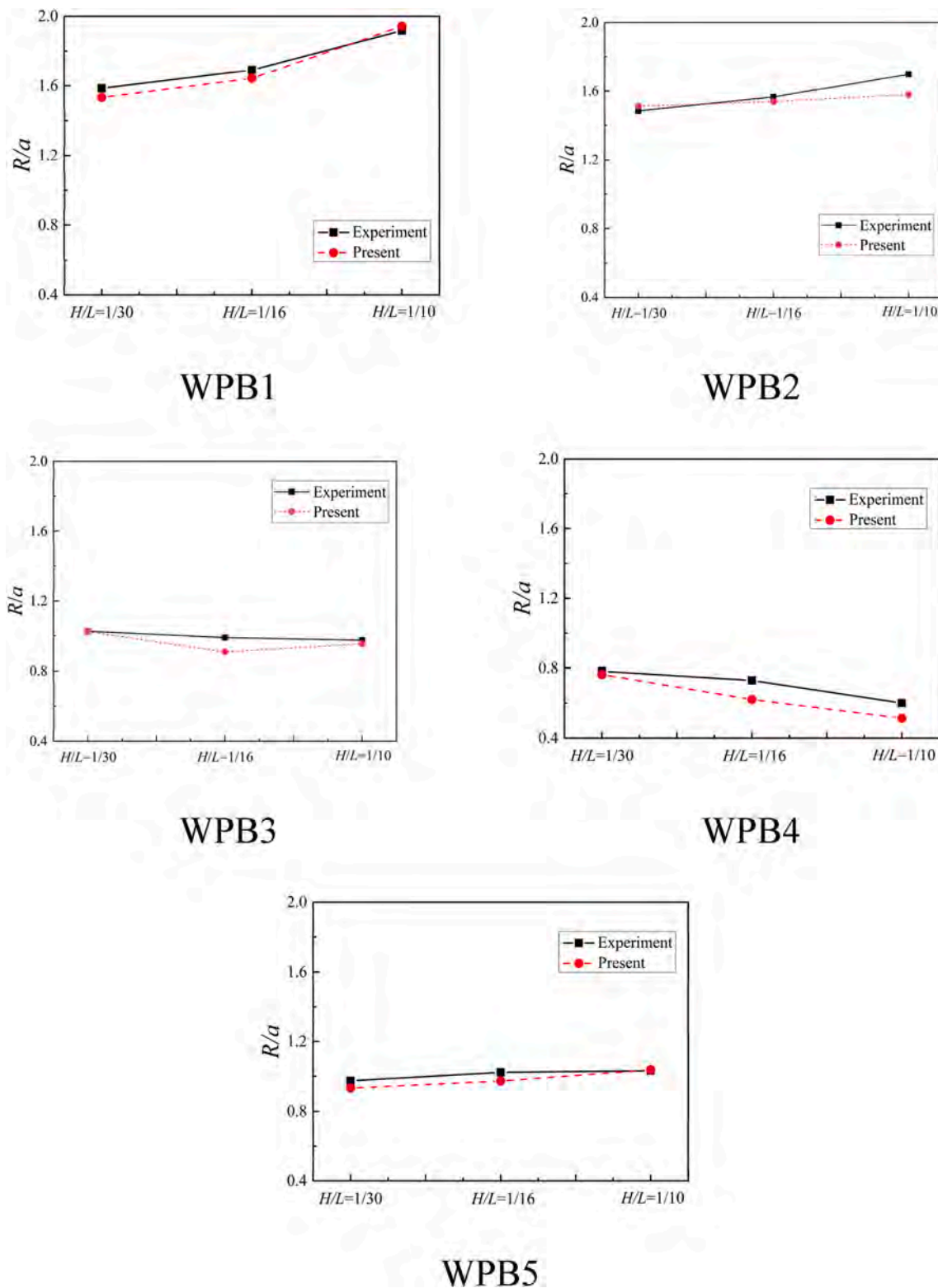
Fig. 6. Comparisons of RAOs of surface elevations near the cylinder for $T = 7s$.

interaction with a vertical surface piercing cylinder. The comparisons between numerical results and physical experimental results indicate that OpenFOAM can accurately model non-linear wave interaction with offshore structures. Based on the open-source platform OpenFOAM, Cao and Wan (2014, 2015; 2017) simulated the regular and solitary waves onto a circular cylinder. The predicted results of wave run-up showed reasonable agreement with theoretical data. Yang et al. (2015)

developed a Modified Marker-Density (MMD) method to predict the wave run-up around a circular column in regular waves. The numerical results were compared to the experimental data and showed good agreement. Sun et al. (2016) used potential flow solver DIFFRACT and viscous flow solver OpenFOAM to investigate non-linear interactions between regular waves and a single truncated circular column. The predicted free surface elevation around the column and the wave forces
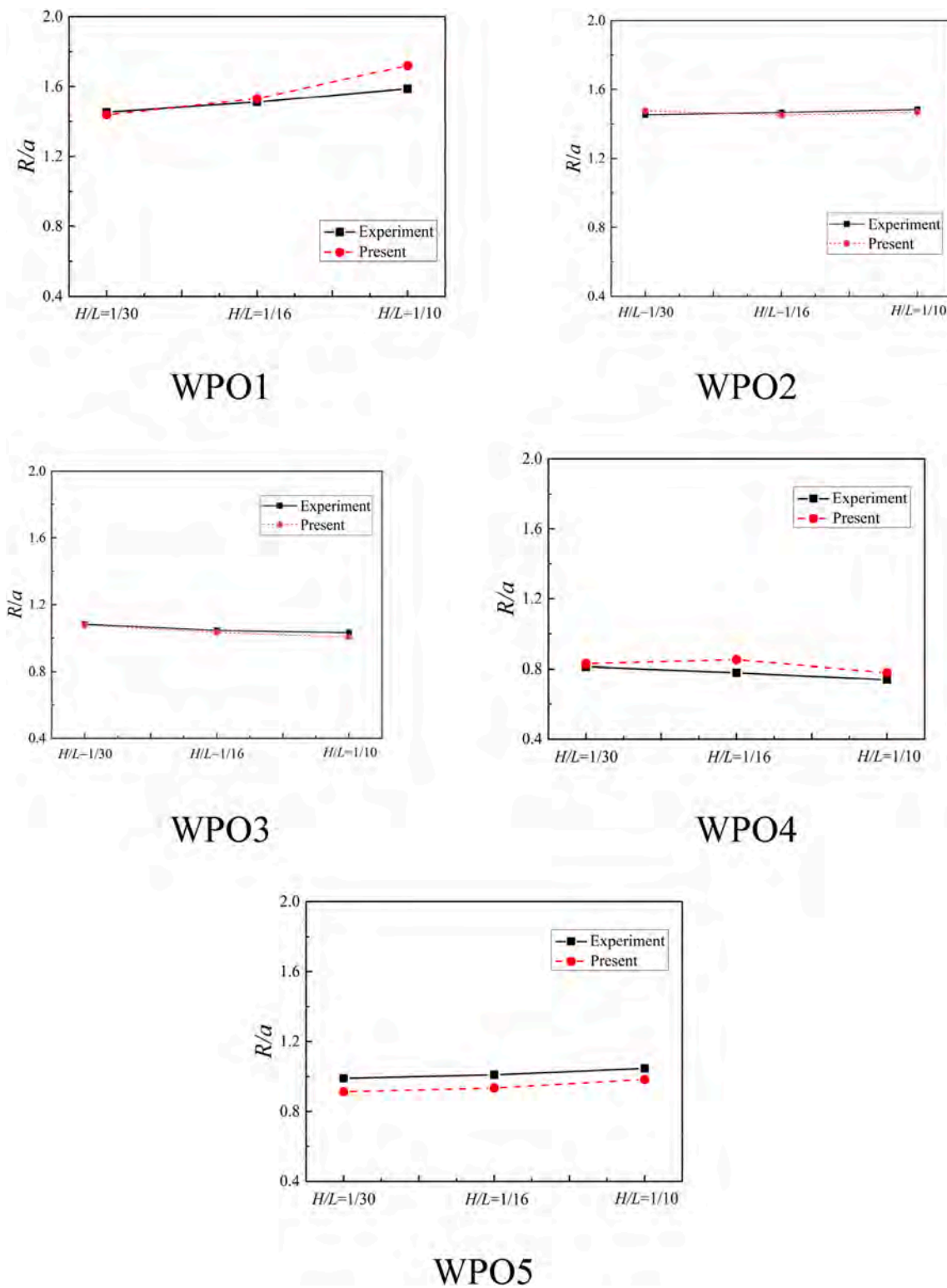
Fig. 7. Comparisons of RAOs of surface elevations away from the cylinder for $T = 7$s.

were analyzed and compared with experimental data. Hu et al. (2016) used OpenFOAM solver to simulate wave-structure interactions and developed a new wave boundary condition for extreme wave generation. Lin et al. (2017) developed a CFD model based on commercial software FLUENT to study the run-up heights accompanied with wave loads by comparing wave steepness parameter and scattering parameter for three different types of wind turbine foundations. Mohseni et al. (2018) used IHFOAM to study wave run-up problems. They found that

the harmonic analysis for both short and longwave cases indicated that the scattered wave field around the cylinder involves high harmonics wave run-up. It was confirmed that even the wave-structure interaction caused by the linear incident wave could lead to weakly non-linear wave amplification around the cylinder. Corvaro et al. (2019) carried out both experimental and numerical studies to analyze the hydrodynamics of a vertical pile in waves. The comparison between experimental and numerical results is provided in velocity, pressure distributions around the
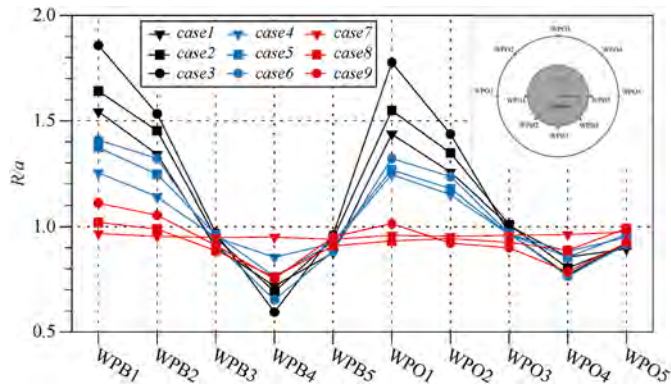
Fig. 8. The RAOs of each wave probe in test cases.
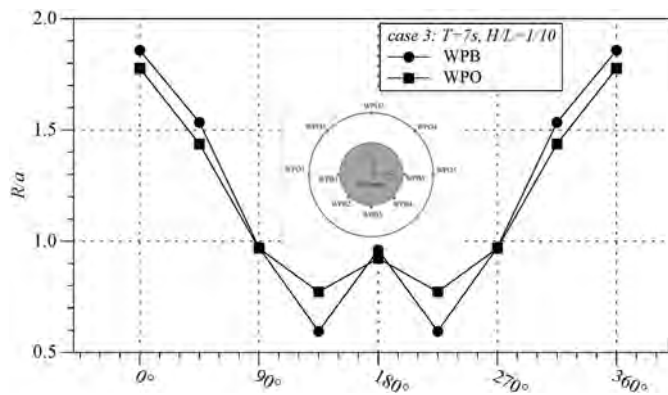
Fig. 9. The RAOs of each wave probe around the cylinder in case 3.

cylinder and total force. They found that the wave action was responsible for an oscillating flow with weak turbulence confined in the pile region.

The interaction between wave and cylinder has attracted much attention. Many researchers have studied this problem from different points of view. The outcome of the studies indicates the importance of high-order nonlinearities and the need for computational efforts for accurate predictions (Hu et al., 2016; Mohseni et al., 2018). The objective of the present work is to give a systematic analysis of the wave run-up on a single fixed cylinder which included wave field types, transient phase difference around the cylinder, and high-order harmonics in wave forces and wave elevations. The numerical results of the free surface elevation around the column and the wave forces are presented and compared with experiments performed at MOERI (Kristiansen et al., 2004). Compared with the single-cylinder case, two tandem cylinders' horizontal forces and surface elevation are displaced and discussed. Then the wave interaction with two tandem cylinders for different center-to-center distances is simulated. The effects of center-to-center distance on wave run-up, wave force, and wave scattering are also presented in this work.

This paper is organized as follows. In Section 2, the numerical method used is presented, including governing equations, VOF method, numerical wave tank, discretization schemes and cylinder fixation. The interaction between regular waves and a single cylinder is investigated in Section 3, which includes: grid convergence study, validations with experiment data, RAO analysis, wave force analysis and flow field analysis. Section 4 describes the wave interaction with two tandem cylinders. Conclusions are provided in Section 5.

2. Numerical methods

2.1. Governing equations

The CFD solver naoe-FOAM-SJTU solves the incompressible unsteady Reynolds-Averaged Navier-Stokes (uRANS) equations for unsteady turbulent flows with the VOF method capturing free surface around the marine structure (Shen et al., 2015; Shen and Wan, 2016; Wang and Wan, 2016; Ye and Wan, 2017). Compared to the OpenFOAM standard solver, the naoe-FOAM-SJTU solver is complemented with a wave generation and damping module, a wave probe module, a six-DoF motion module, a mooring system module, and turbulence models. The governing equations of incompressible viscous fluids in the present solver are as follows:

$$\nabla \cdot U = 0 \tag{1}$$

$$\frac{\partial \rho U}{\partial t} + \nabla \cdot \left(\rho \left(U^2 \right) \right) = -\nabla p_d - g \cdot x \nabla \rho + \nabla \cdot \left(\mu_{eff} \nabla U \right) + \left(\nabla U \right) \cdot \nabla \mu_{eff} + f_\sigma + f_s \tag{2}$$

where U is the velocity field. $p_d = p - \rho g \cdot x$ is the dynamic pressure, and p is the total pressure. ρ is the mixed density of the two phases water and air. μ_{eff} is the effective dynamic viscosity, in which ν and ν_t are kinematic viscosity and eddy viscosity, respectively. f_σ is the surface tension, which impacts the free surface. f_s is a source term added to generate the sponge layer for wave absorbing.

2.2. The capture of free surface

The free surface of the two-phase flow is captured by the VOF method (Hirt and Nichols, 1981) with artificial bounded compression techniques. The method is based on a volume fraction α which can control numerical diffusion and capture the interface with high resolution. The volume fraction function can be determined by solving a transport equation:

$$\frac{\partial \alpha}{\partial t} + \nabla \cdot \left[(U - U_g) \alpha \right] + \nabla \cdot [U_r (1 - \alpha) \alpha] = 0 \tag{3}$$

The first two terms on the left-hand side of Eq. (3) stand for the traditional volume of the fluid transport equation, while the third term represents the artificial compression term. The compression velocity U_r (Weller et al., 1998) is computed at cell faces by the maximum velocity magnitude at the interface region:

$$U_{r,f} = n_f \min \left\{ C_\alpha \frac{|\varphi|}{|S_f|}, \max \left(\frac{|\varphi|}{|S_f|} \right) \right\} \tag{4}$$

where ϕ is face volume flux; C_α is a compression coefficient controlling the magnitude of compression. In this paper, it is chosen to be 1.0. A larger value will increase the compression of the interface, leading to larger detrimental velocity gradients around the interface. The compression term only works on the interface without affecting the numerical computation out of the transition layer due to term $(1 - \alpha) \alpha$.

Different phases are marked using volume fraction α, which indicates the relative proportion of fluid in each cell. It is defined as Eq. (5). For an interface cell, the value of volume fraction α is between 0 and 1, representing it contains both water and air.

$$\begin{cases} \alpha = 0 & \text{air} \\ \alpha = 1 & \text{water} \\ 0 < \alpha < 1 & \text{interface} \end{cases} \tag{5}$$

In the physical domain, the density of fluid ρ and the dynamic viscosity μ can be obtained by a weighted value based on the volume fraction α:

$$\rho = \alpha \rho_1 + (1 - \alpha) \rho_2 \tag{6}$$
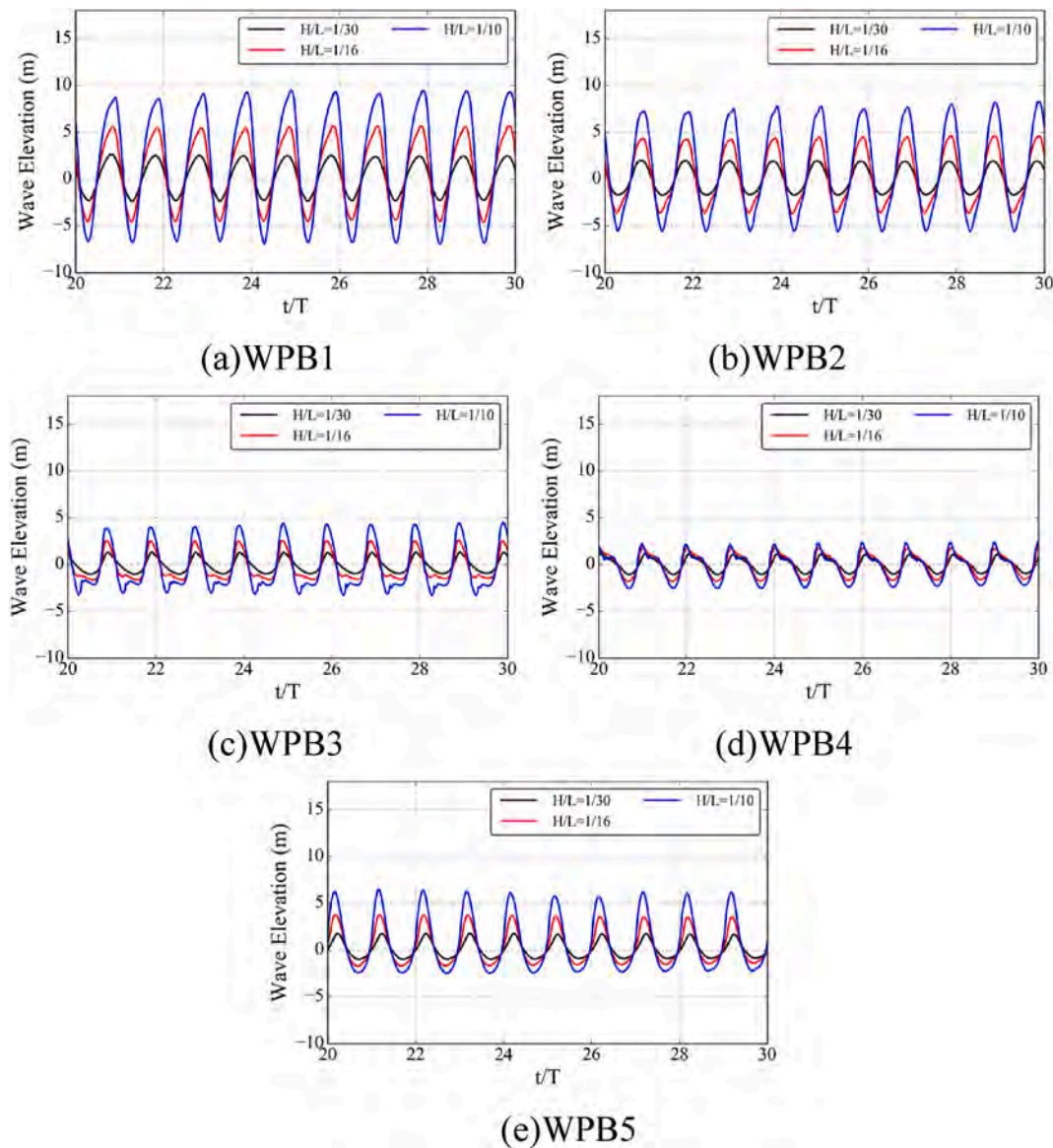
Fig. 10. Time series of surface elevation for inner circle wave probes for $T = 7$s.

$$\mu = \alpha\mu_1 + (1 - \alpha)\mu_2 \tag{7}$$

where ρ_1 and ρ_2 denote the density of water and air, μ_1 and μ_2 denote the viscosity coefficient of water and air, respectively.

2.3. Numerical wave tank

A wave generation, probing and damping modules have been extended to the in-house naoe-FOAM-SJTU solver, as shown in Fig. 1. The velocity inlet wave-making method is adopted to generate regular or irregular waves. To generate the Stokes first deep-water wave, the inlet boundary conditions are set as follows:

$$\eta = a \cos(\mathbf{k} \cdot \mathbf{x} - \omega_e t + \delta) \tag{8}$$

$$u = a\omega e^{kz} \cos(\mathbf{k} \cdot \mathbf{x} - \omega t + \delta) \tag{9}$$

$$v = a\omega e^{kz} \cos\beta \cos(\mathbf{k} \cdot \mathbf{x} - \omega t + \delta) \tag{10}$$

$$w = a\omega e^{kz} \sin\beta \sin(\mathbf{k} \cdot \mathbf{x} - \omega t + \delta) \tag{11}$$

where η is transient wave elevation, a, ω and $\mathbf{k}$ are wave amplitude, wave frequency and wavenumber, respectively. β represents wave incident direction.

To avoid wave reflection, a sponge layer is set at the outlet of the computational domain. The term of f_s is introduced into Eq. (2) for absorption of waves and defined as:

$$f_s(x) = \begin{cases} -\rho\alpha_s \left(\dfrac{x - x_s}{L_s}\right)^2 (U - U_{ref}) & \text{inside sponge layer} \\ 0 & \text{outside sponge layer} \end{cases} \tag{12}$$

The α_s is an artificial viscosity coefficient controlling the intensity of the sponge layer, which is set to be 20. The x_s is the coordinate of the start position of the sponge layer, and L_s is the length of the sponge layer. The source term f_s has no effects on the domain out of the sponge layer.

2.4. Discretization schemes

In the naoe-FOAM-SJTU solver, the RANS and VOF transport equations are discretized by the finite volume method (FVM). Van Leer scheme is applied for the VOF equation in OpenFOAM. The naoe-FOAM-SJTU solver employs a segregated method named PIMPLE to decouple
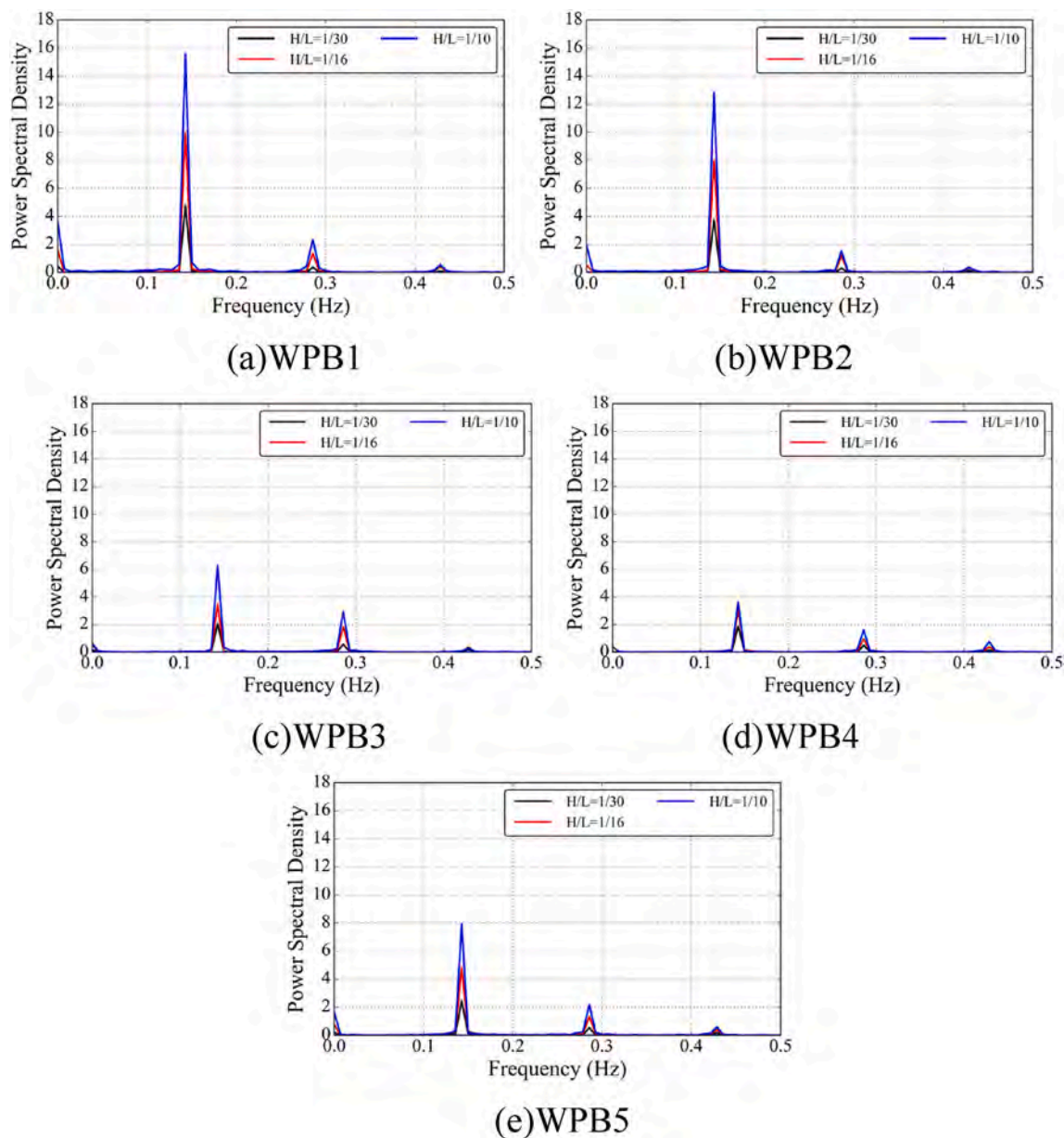
Fig. 11. FFT of surface elevation for inner circle wave probes for $T = 7$s.

velocity and pressure. PIMPLE is a combination of the SIMPLE and PISO algorithm provided by OpenFOAM. When advancing to a new time step, the solver first updates mesh, then solves momentum equations to get an intermediate velocity used to construct the pressure Poisson equation later. After that, the solver enters the PISO loop, solves for pressure, and performs non-orthogonal correction several times. Then the velocity and flux are corrected, and the solver enters the next SIMPLE iteration. The convection terms are solved by a second-order TVD limited linear scheme, which is generalized for unstructured mesh. The diffusion terms are approximated by a second-order central difference scheme to ensure conservation. Detailed information can be referred to Greenshields (2018).

2.5. The cylinder fixation

In the in-house naoe-FOAM-SJTU solver, we have a six degree-of-freedom module to control the motion of the cylinder. The motion of the cylinder in each degree-of-freedom can be set as fixed or moving. In our simulation, the motion of the cylinder in each degree-of-freedom is

set as fixed. Detailed information about the six degree-of-freedom module can be found in Wang et al., (2019). Although the paper that illustrated the experiment does not detail how the cylinder is fixed, we find that in similar experiments, the cylinder is permanently fixed with the load cell at the upper side. So no movement or vibration can be found for the cylinder in the experiment. We consider that our numerical model can replicate the experiment for cylinder fixation.

3. Wave interaction with single cylinder

3.1. Computational model

To simulate wave run-up on a single truncated surface-piercing cylinder, the cylinder model at full scale from MOERI is selected in the present work (Kristiansen et al., 2004; Sun et al., 2016). The diameter of the cylinder is $D = 16.0$ m, and the draft is 24.0 m. A series of wave probes in both experiment and numerical simulation are placed around the cylinder, as shown in Fig. 2. The corresponding location is given in Table 1. The distances from the cylinder center to inner circle
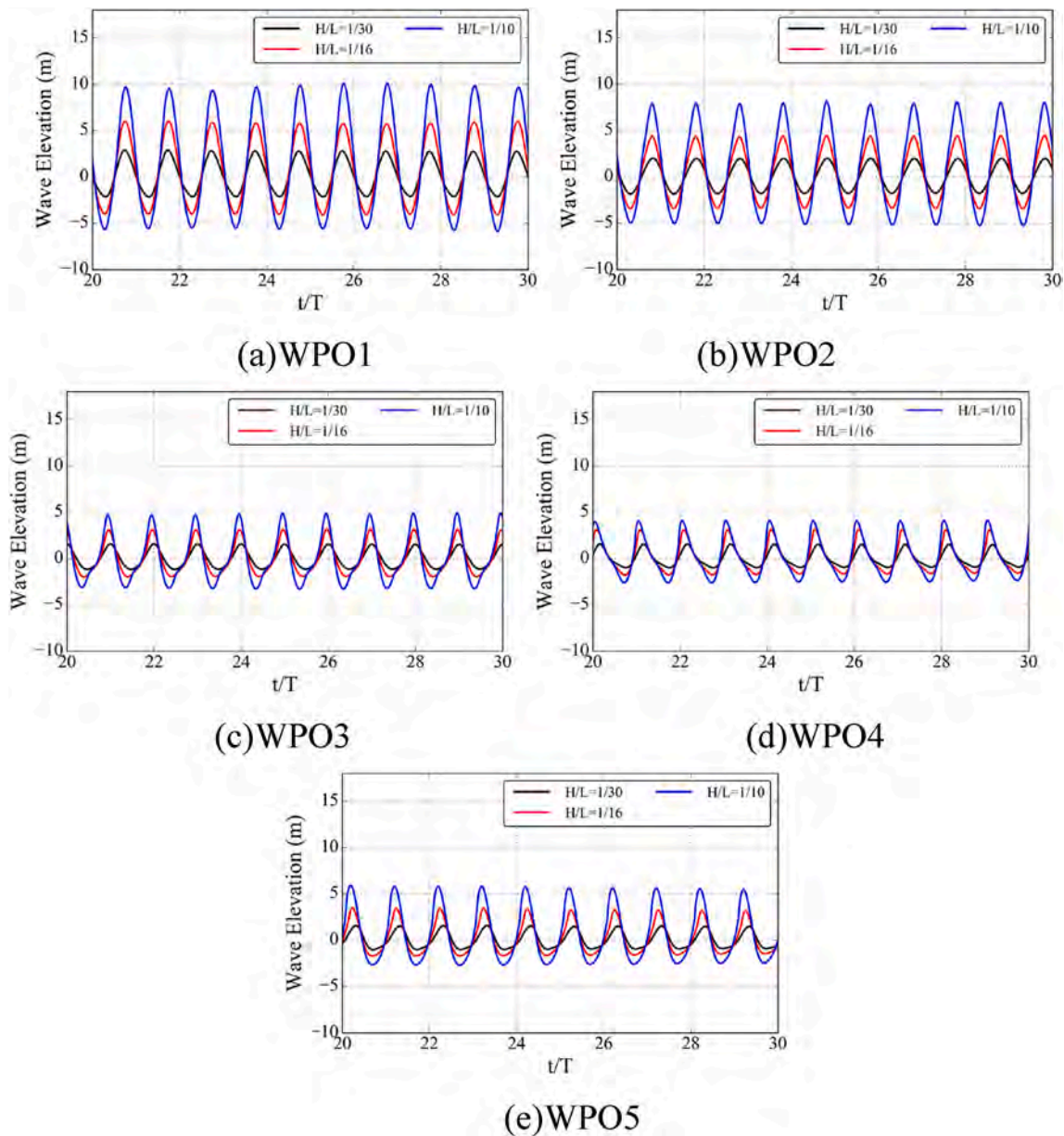
Fig. 12. Time series of surface elevation for outer circle wave probes for $T = 7$s.

wave probes and outer circle wave probes are 0.2063 m and 8 m, respectively.

Fig. 3 shows the arrangement of the computational domain. The domain extends to $-2L < x < 3L$, $-L < y < L$, $-L < z < 0.5L$. Where L represents the wavelength. The water depth is set as one wavelength L. The length of sponge length is also set as L, starting from $x = 2L$. The vertical cylinder is fixed at the center of the wave tank.

The computational mesh is shown in Fig. 4. About 80 grids per wavelength and 20 per wave height are applied in the present work. To make it easy to converge in each time step, the interface Courant number was controlled to be under 0.3. The time step is 0.005s in each case. The boundary conditions are as follows: Velocity inlet boundary condition is adopted. Zero-Gradient condition is applied at the outlet. The no-slip boundary condition is imposed on the cylinder. The symmetry boundary condition is applied to the side walls.

3.2. Test conditions

The incident wave conditions were set according to the benchmark

study conditions proposed by the 27th ITTC committee. The Stokes first-order deep water wave is applied in the present work. Three wave periods ($T = 7$s, 9s, and 15s) have been investigated. Three steepness parameters ($H/L = 1/30$, 1/16, and 1/10) were simulated for each wave period, where H is the wave height, and L is the wavelength. Another parameter in our analysis is the scattering parameter $k_0 r$, where k_0 ($k_0 = 2\pi/L$) is the wavenumber. KC (Keulegan-Carpenter) number is defined as $KC = \pi A/D$, where A is wave amplitude, and D is the cylinder diameter. Details of the test conditions are listed in Table 2.

3.3. Grid convergence study

A grid convergence study is a straightforward and consistent way to determine the magnitude of discretization error in numerical simulation. This paper performs grid convergence examinations for $T = 7$s and $H/L = 1/30$ without cylinder. According to the experiments, the errors arising from extrapolation can be reduced if the refinement ratio of $r > 1.3$ (Hajivand and Mousavizadegan, 2015). In this study, a refinement ratio of $r = \sqrt{2}$ in each direction is selected. The refinement ratio is

(a)WPO1

(b)WPO2

(c)WPO3

(d)WPO4

(e)WPO5
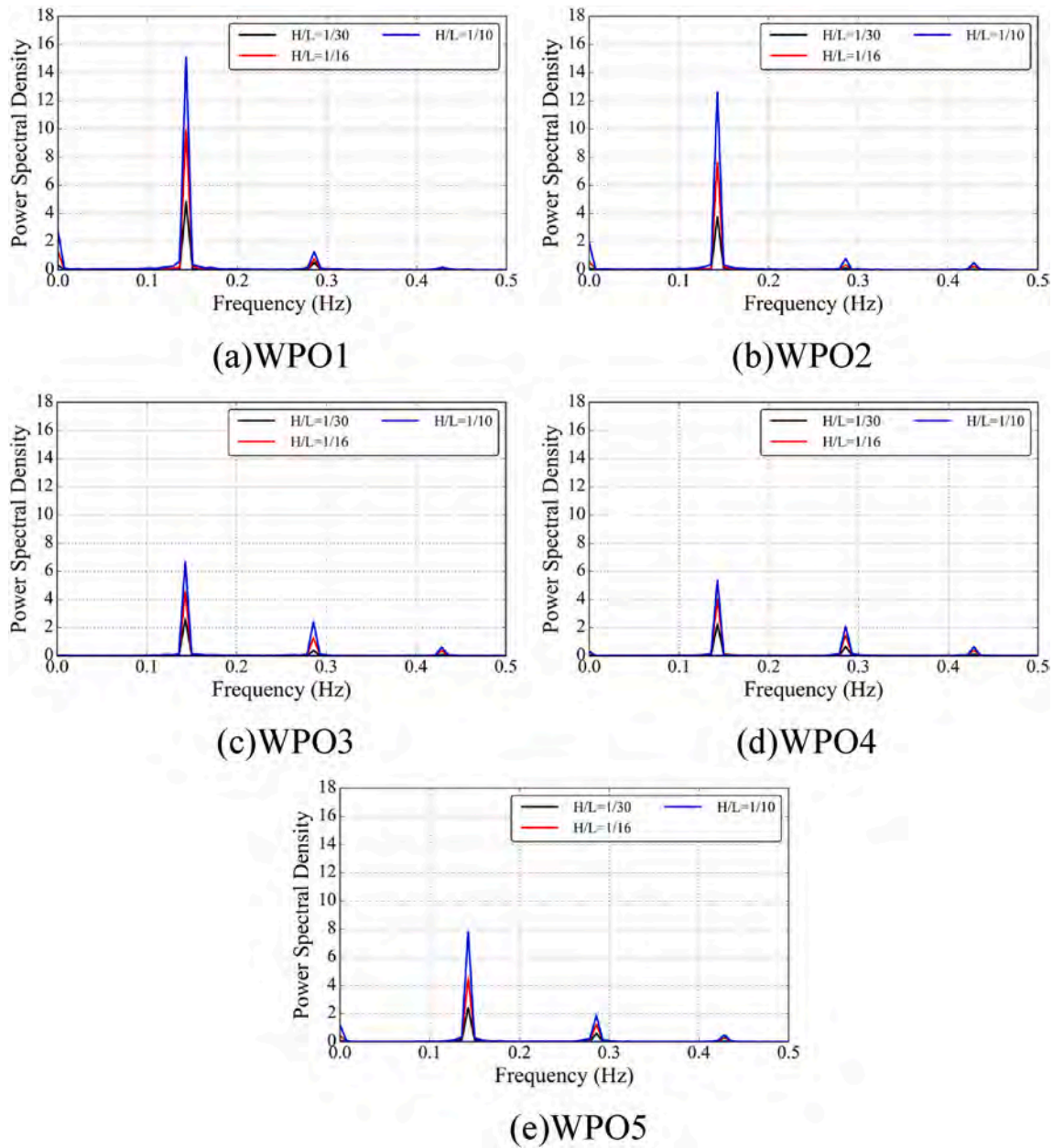
Fig. 13. FFT of surface elevation for outer circle wave probes for $T = 7$s.

defined as the fine mesh number to the coarse mesh number. The total number of coarse mesh (mesh1), medium mesh (mesh2), and fine mesh (mesh3) are 1.01M, 2.01M, and 4.02M, respectively. The time histories of surface elevations at WPB1 for the three meshes and theory are shown in Fig. 5. Few differences can be found in the numerical results for the medium and fine meshes. The results of coarse mesh show more significant differences than medium and fine meshes, relatively. The error between numerical and experimental results is 2.5% for the fine mesh condition, consistent with the medium mesh condition. For coarse mesh condition, the error is 4.6%. The medium mesh is used as the background mesh for the remaining simulations.

Then, a grid convergence study for wave elevations with cylinder and forces acting on the cylinder has been carried out to prove the computation is converged in our study. For case 1, three different background meshes used in the wave-only case above are adopted here. The total numbers of coarse, medium and fine mesh are 1.41M, 2.51M, and 4.72M, respectively. The time step is 0.005 s in each case. To quantitatively estimate uncertainty due to grid and time step errors, we

adopt a verification method proposed by Stern et al. (2006). The convergence solution (R_G) of different solutions (S_i) is defined as:

$$R_G = \frac{S_2 - S_1}{S_3 - S_2} \tag{13}$$

where S_i corresponds to solutions with fine, medium, and coarse grids, respectively. The different R_G values represent different convergence conditions: (1) $0 < R_G < 1$ represents monotonic convergence, and generalized Richardson extrapolation (RE) is used to estimate grid uncertainty. (2) $R_G < 0$ represents oscillatory convergence, and uncertainties can be estimated by attempting to bound the error based on oscillation maximums S_U and minimums S_L. (3) $R_G > 1$ represents divergence, and uncertainties cannot be estimated. In our study, the results show good convergence, as summarized in Table 3. As the grid is refined, the maximum crest of wave elevation approaches the experimental data monotonically. Thus, the RE method is used to estimate the convergence rate in this study (Roache, 1994). Order of discretization estimated as follows:
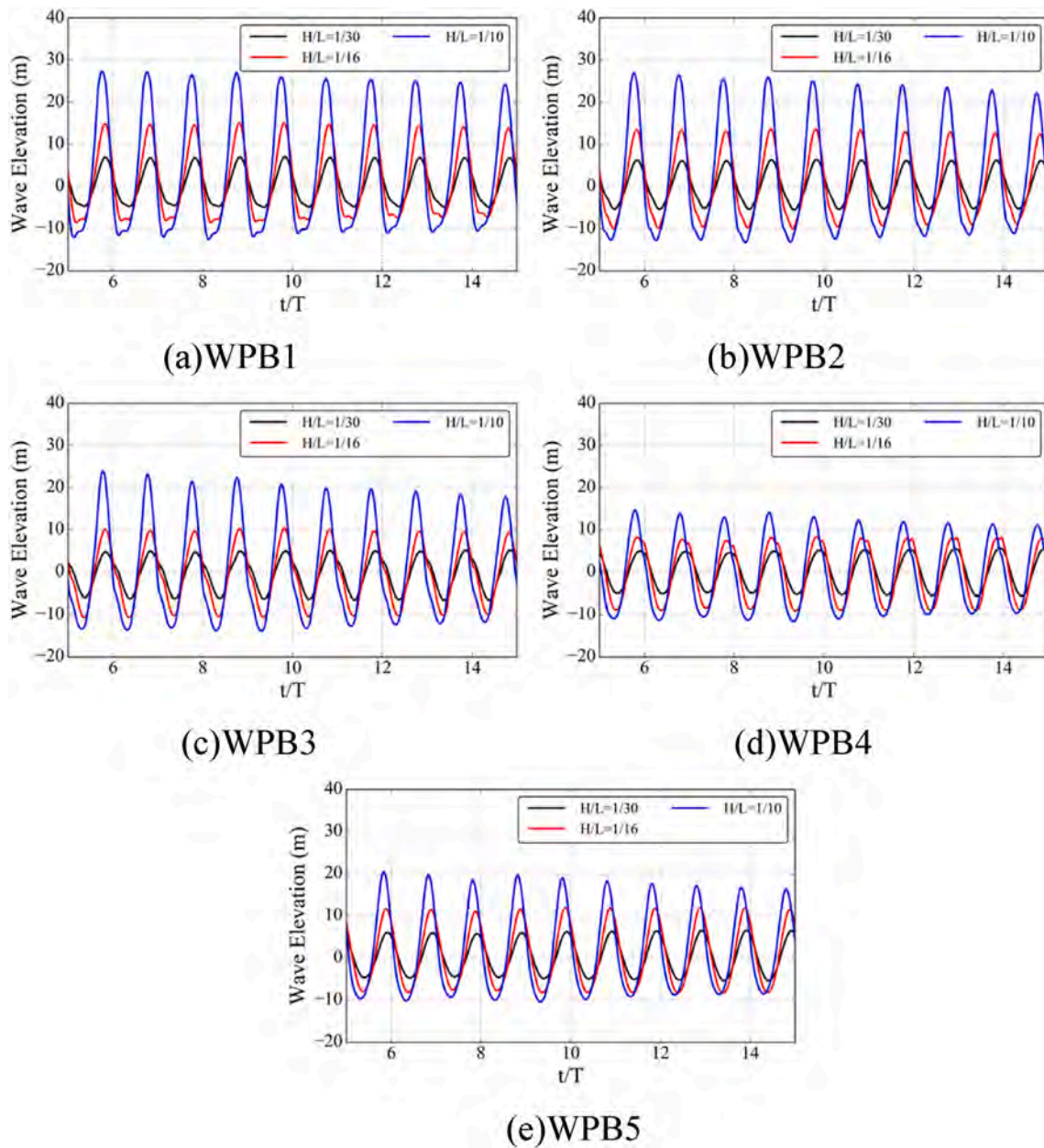
Fig. 14. Time series of surface elevation for inner circle wave probes for $T = 15s$.

$$P = \frac{\ln(1/R_G)}{\ln(r)} \tag{14}$$

then, Grid Convergence Index (GCI) is defined:

$$GCI_{ij} = F_S \frac{|e_{ij}|}{r^p - 1} \tag{15}$$

where F_S is a safety factor, and for convergence study with a minimum of three grids or more, $F_S = 1.25$ according to Roache (1994), e_{ij} is the error between S_i and S_j. The GCI can indicate the error using different grids. A small value of GCI means the solution is accurate relatively. Table 3 shows the GCI values of RAO at WPB1 and normalized first-order horizontal wave force. As shown in Table 3, the RAO at WPB1 shows monotonic convergence with R_G of 0.157. The GCI_{12} (between fine and medium) of the RAO at WPB1 is only 0.28%, illustrating that grid density has a limited effect on wave elevation for the fine and medium grids. It is evident that the value of GCI_{23} (between medium and coarse) is larger than that of GCI_{12}. The error of RAO at WPB1 between coarse

grid and experimental results is much larger than that of the medium and fine grids. The normalized first-order horizontal wave forces for different meshes are also shown in Table 3. The first-order horizontal wave force shows monotonic convergence with R_G of 0.269. The GCI_{12} and GCI_{23} for wave force show a similar trend as GCI_{12} and GCI_{23} for RAO at WPB1. The grid uncertainty between the simulation results of the fine grid and the medium grid is under 1%, but the computational time is significantly increased. The medium grid is selected in our study.

3.4. Comparisons with experimental data

The response amplitude operates (RAOs) are effectively transfer functions used to determine the effect of waves on the offshore structures. The CPU time per wave period is about 5.64 h. The calculated time histories of the free surface elevation of wave loadings are generally adopted to acquire the RAOs using the Fast Fourier analysis, which is the average wave elevation divided by the original wave elevation. The acquired RAOs of free surface elevations at wave probe locations from
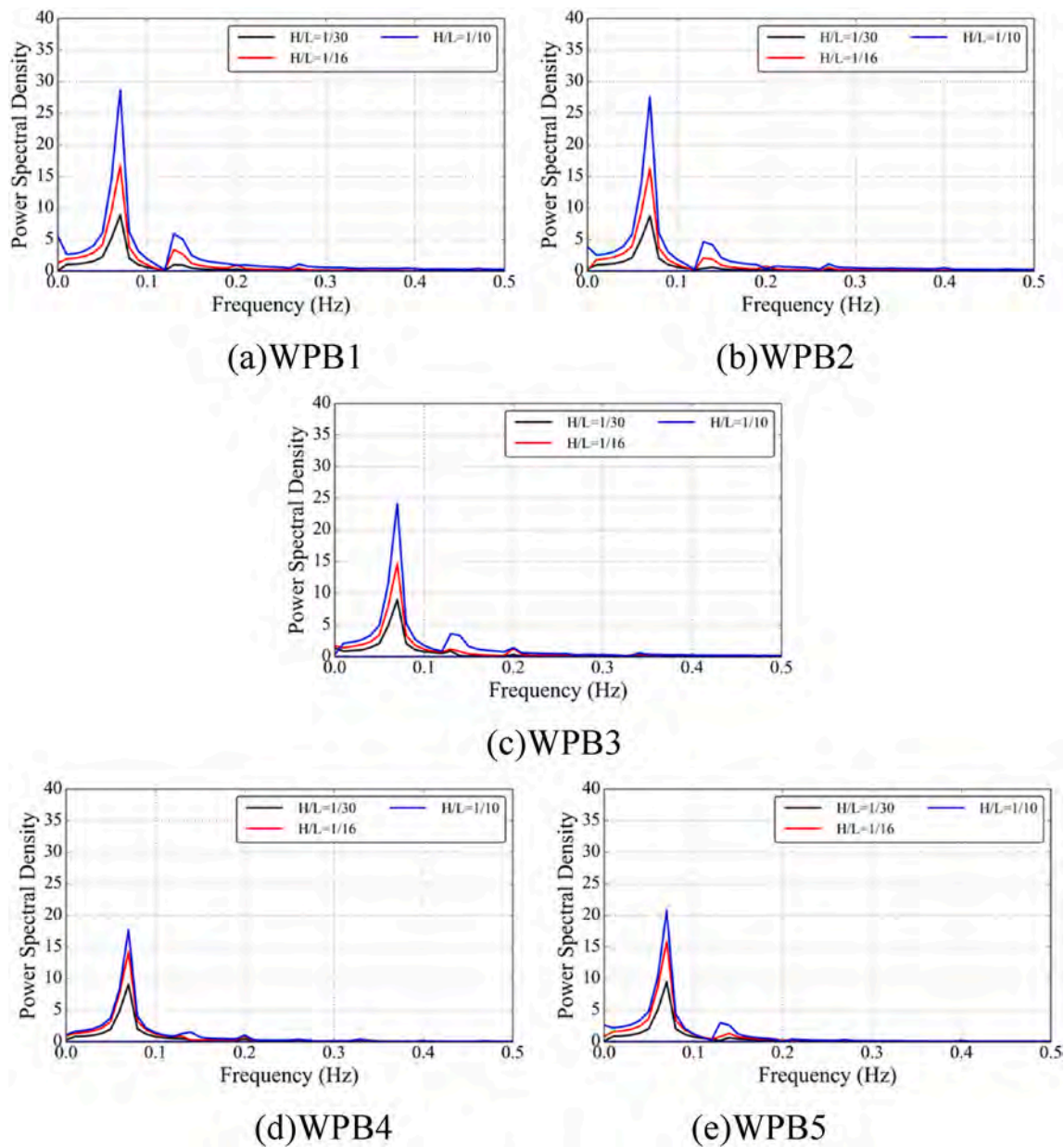
Fig. 15. FFT of surface elevation for inner circle wave probes for $T = 15$s.

our CFD simulation are compared with the experimental data from MOERI (Kristiansen et al., 2004). Fig. 6 and Fig. 7 show the comparisons of the RAOs of surface elevation near the cylinder and away from the cylinder for the cases $T = 7$s, respectively.

As shown in Figs. 6 and 7, the CFD results agree well with the experimental data for the wave probes in front of the cylinder. With the increase of wave steepness, the RAO value at WPB1 increases. This agrees well with experimental data. At WPO1, it shows the same phenomenon that the wave run-up increases with wave steepness, but the value of the increase is slightly smaller than that of experimental results. In the meantime, the RAO values of any wave steepness at WPO1 are smaller than that in front of the cylinder. At WPB2 and WPO2, the RAO

value shows a similar trend as the value at WPB1. At WPB3 and WPO3, the RAO value is around 1. At WPB4, which displaces an inclined rear position near the cylinder, the value of RAO is around 0.8. The trends of decrease with the increase of wave steepness are not prominent. This is consistent with that in experiments. The RAOs at WPB4 and WPO4 are all smaller than 1, which illustrates that the wave elevation is smaller than the original one and shows no wave run-up. In the position behind the cylinder, the RAO value of WPB5 and WPO5 is around 1, which shows an inapparent wave run-up at the rear of the cylinder. Reasonable agreement between the CFD results and experimental data implies that the present solver is capable of predicting the wave run-up on a truncated cylinder.
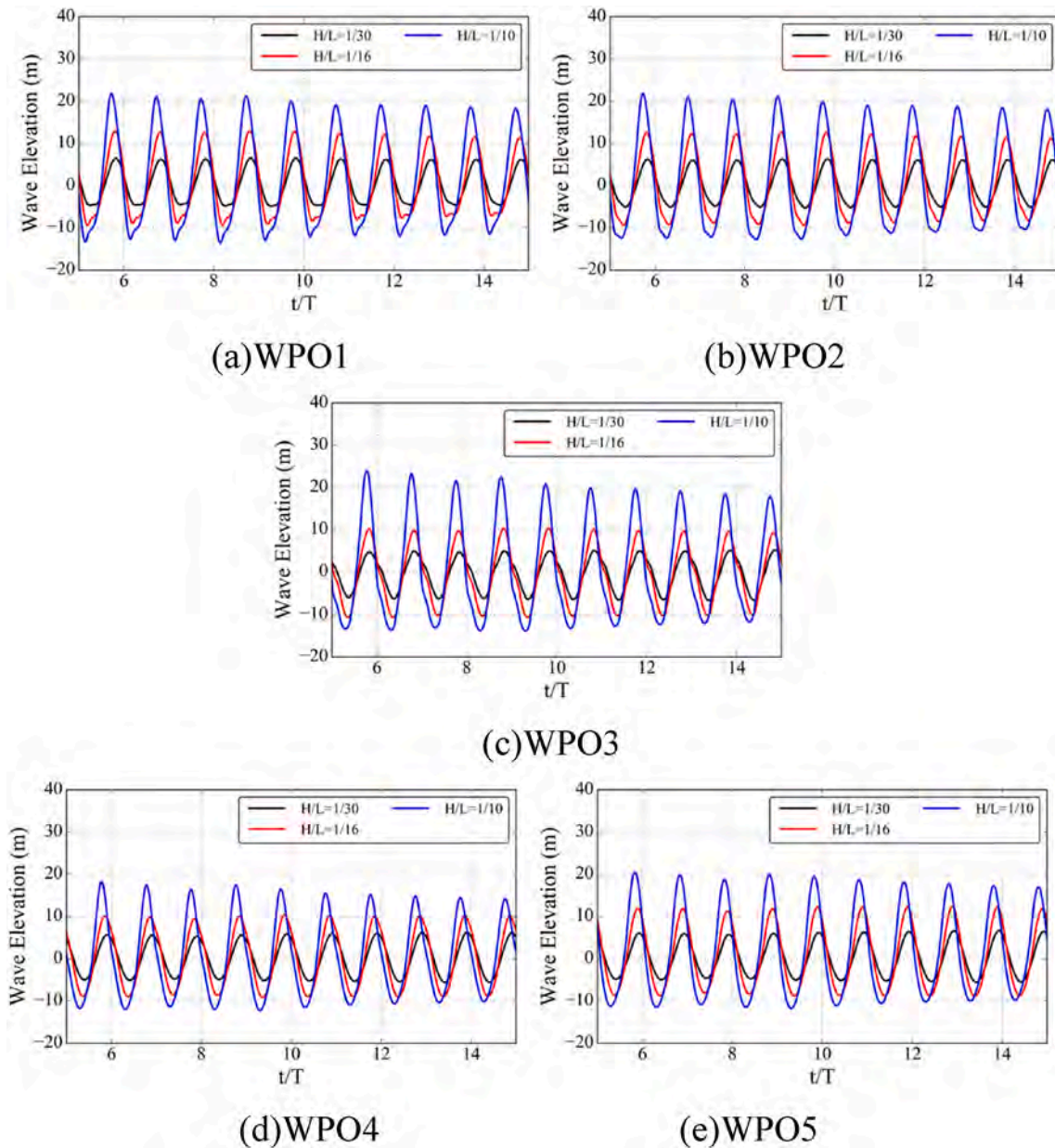
Fig. 16. Time series of surface elevation for outer circle wave probes for $T = 15$s.

3.5. The analysis of RAO of free surface elevation

Fig. 8 shows the RAOs in 10 wave probes of 9 test cases. The black line stands for the condition of wave period $T = 7$s, the blue line stands for $T = 9$s, and the red line stands for $T = 15$s. The triangle mark presents for wave steepness $H/L = 1/30$, the square mark presents $H/L = 1/16$, and the circle mark presents $H/L = 1/10$. The horizontal ordinate corresponds to the position of wave probes, the vertical ordinate is RAO, and the value of R/a in each wave probe is the highest wave amplitude in ten steady wave periods divided by the regular wave amplitude.

Fig. 8 shows that the change of value in cases of the smallest wave period is most apparent. The ratio of RAO in highest wave steepness (case 3) reaches the value of 6 times (WPB1:WPB4); with the increase of

the wave period, the difference of RAO in the same test condition decreases. In the condition of case 7 ($T = 15$s, $H/L = 1/30$), the RAO of 10 wave probes shows a trend of one line, and the value is around 1. This illustrates that the cylinder has no influence on waves for case 7.

For the different wave steepness cases, for example, when $T = 7$s, the RAOs of WPB1 and WPB2 increase with the rise of wave steepness; the RAOs of WPB3 and WPB5 is around 1, varies a little with the wave steepness; the RAOs of WPB4 decrease with the increase of wave steepness, $R/a \approx 0.6$ when the wave steepness reaches the highest. It shows the same feature in five WPO wave probes. For different wave period conditions, for example, when $H/L = 1/10$, the wave period influence well on RAOs, the cylinder affects the wave the most when the wave period is the smallest. When considering the KC number, the larger
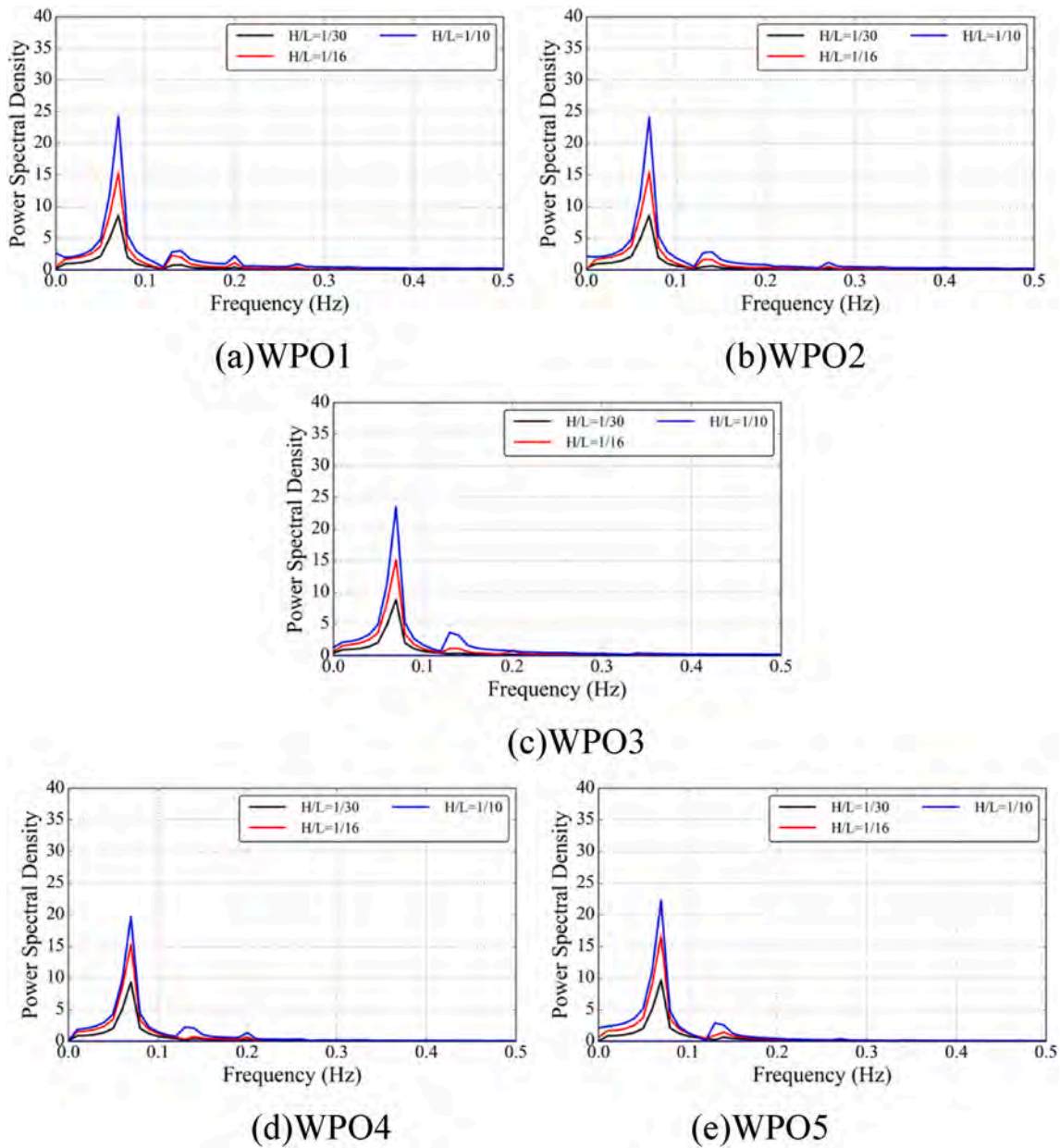
Fig. 17. FFT of surface elevation for outer circle wave probes for $T = 15$s.
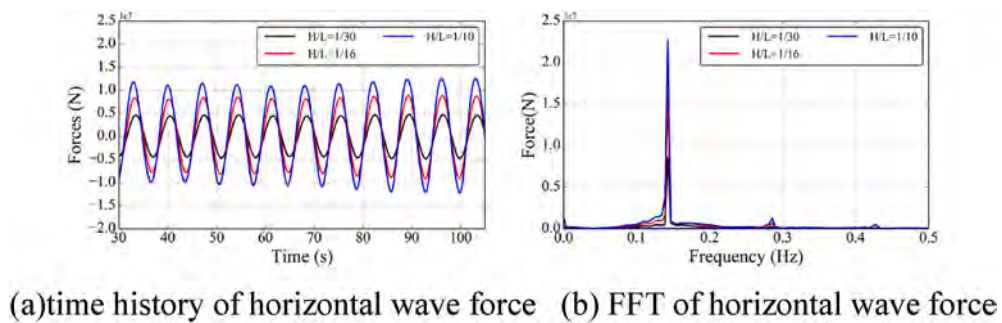
Fig. 18. Time series and FFT of horizontal wave force for $T = 7$s.
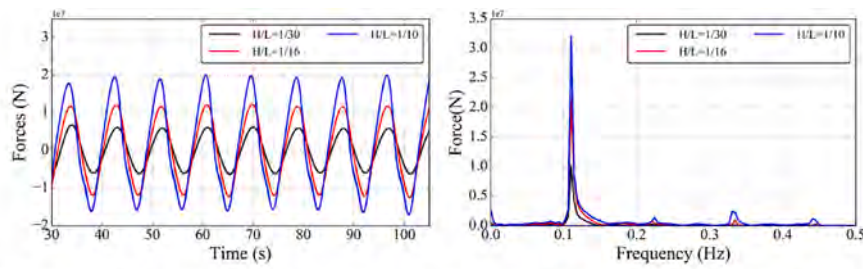
(a)time history of horizontal wave force   (b) FFT of horizontal wave force

Fig. 19. Time series and FFT of horizontal wave force for $T = 9s$.
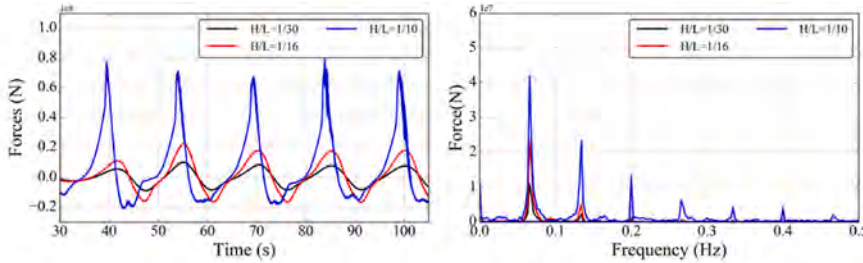
(a)time history of horizontal wave force (b) FFT of horizontal wave force

Fig. 20. Time series and FFT of horizontal wave force for $T = 15s$.

the *KC* number indicates the smaller wave run-up on the front of the cylinder and the smaller wave depress on the rear of the cylinder.

Fig. 9 shows the RAOs around the cylinder in case 3. The circle marks represent the values of RAOs near the cylinder, while square marks represent the values of RAOs far away from the cylinder. The wave run-up shows symmetrical displacement around the central axis of wave propagation, shows a shape of "W" around the cylinder. Because of the run-up effects, RAO reaches the largest in the wave-facing position in front of the cylinder. In the process of incident wave propagation from the sides of the cylinder to the back of the wave, due to the wave scattering effects and the viscous effects on the wake flow of the cylinder, the energy waste in the wave decreases. This causes the separation vortex on the backside of the cylinder. It can be seen from Fig. 8, the lowest wave run-up position appears on the back of the cylinder, presents 135° from the facing-wave position of the cylinder (WPB4, WPO4). The wave run-up is caused by two reasons: the scattering effects due to wave-structure interaction and viscous effects on the wake flow of the cylinder. Therefore, the smallest wave run-up appears on WPB4 and WPO4. This may be due to the influence of the vortex, which is formed from incident waves and viscous effects.

3.6. Time histories of free surface elevation

For the wave period $T = 7s$ condition, time histories of the free surface elevation obtained from our CFD simulation are shown in Fig. 10 (inner circle probes) and Fig. 12 (outer circle probes). Fast Fourier transform was conducted to get harmonics of free surface elevation. The corresponding FFT results are shown in Fig. 11 (inner circle probes) and Fig. 13 (outer circle probes). As shown in Fig. 10, the water in front of the cylinder (at WPB1) reaches the largest wave amplitude in any wave height condition. This is because when the wave crest reaches the

cylinder, the water is blocked and runs up vertically along with the cylinder. The surface elevation at WPB1 can be two times the incident wave amplitude. The surface elevation at the downstream quarter-point WPB4 is the smallest, and secondary crests can be found for steeper waves ($H/L = 16$ and $1/10$), which can be clearly seen from the FFT analysis. This may imply strong non-linear interaction at this location. After passing the sides of the column, the incident wave encounters and interferes with each other, resulting free water flows backward in the upstream direction and overlaps with the incident wave. Thus, the secondary crest can be observed. Similar trends can be found for outer circle wave probes, as shown in Fig. 12. However, the discrepancies for these wave probes are reduced compared with the inner circle ones. The secondary crests at WPO4 are not so evident as WPB4 near the cylinder.

It can be seen in Fig. 11 that all the probes show high-order components. The nonlinearity of the time history of wave elevation of WPB1 is not apparent; however, the high-order component is shown at WPB1. The first-order component at WPB1 is dominant, while the first-order and second-order component at WPB3 is almost the same. Therefore, the nonlinearity can be seen at WPB3. Meanwhile, the value of WPB3 and WPB5 is almost the same in Fig. 8 but shows a difference in FFT analysis. The value of the first-order harmonic at WPB3 is smaller than that at WPB5. The value of the second-order harmonic at WPB3 is more significant than that at WPB5. Similar phenomena can be found at WPOs.

For the wave period $T = 15s$ condition, time histories of the free surface elevation obtained from our CFD simulation are shown in Fig. 14 (inner circle probes) and Fig. 16 (outer circle probes). The corresponding FFT results are shown in Fig. 15 (inner circle probes) and Fig. 17 (outer circle probes). Comparing to the cases in $T = 7s$, the cases of $T = 15s$ shows a weak non-linear response. As shown in Fig. 14, the wave crest is very thin and sharp compared to the wave trough at WPB1. With

Fig. 21. Free surface elevation at the front and back point of the cylinder vs. horizontal wave force.

in long wavelength and small wave steepness.

3.7. Numerical analysis of wave forces

Fig. 18, Fig. 19 and Fig. 20 show the time histories of horizontal wave force and FFT results for $T = 7s$, $T = 9s$, and $T = 15s$ conditions, respectively. In the case of $T = 7s$, the horizontal wave force increases with the wave height. The nonlinearity in wave force is not as strong as surface elevation. This is because that the local non-linear effects are integrated out when computing the force, while the surface elevation shows the original local nonlinearity of wave run-up the cylinder. Therefore it is essential to study the local free surface near the cylinder. For $T = 9s$, the high order harmonic greatly influences wave force in the large wave steepness condition. When the wave steepness $H/L = 1/10$, the fourth-order of horizontal force appears. The horizontal wave force in $T = 15s$ shows great non-linear features, the wave crest is thin and sharp, and the wave trough is relatively flat in high wave steepness $H/L = 1/10$. It also appears seventh-order wave force. For the medium wave steepness, $H/L = 1/16$ appears second order horizontal wave force.

According to the position of the cylinder in the wave field, the horizontal wave force is mainly caused by the free surface elevation on wave-facing position and back-wave position due to its symmetrical feature. In order to analyze the relationship between the front and back forces, this paper gives the horizontal wave force and surface elevation on the front and back point of the cylinder in 9 cases, shown in Fig. 20. The black line stands for the horizontal wave force on the cylinder; the blue line stands for the free surface elevation at WPB1; the red line stands for the free surface elevation in WPB5. In Fig. 21 (a)~(c) are the three cases in short waves. It illustrates that the phase difference at WPB1 and WPB5 is around 180°; when the free surface elevation reaches the highest level in the front point of the cylinder, the surface elevation is at wave trough in the back point of the cylinder. The curve of wave forces shows little difference between the wave crest and the wave trough. It reaches wave crest before the curve of WPB1 reaches the highest level. In Fig.21 (e)~(f), the phase difference between free surface elevation at WPB1 and WPB5 is around 120°, the curve of wave force is regular. In Fig.21 (g)~(i), the phase difference between free surface elevation at WPB1 and WPB5 is around 20°, the nonlinearity in wave forces is more evident than that in short wave and medium wave cases. The non-linear aspect in free surface elevation is not shown by the difference between the wave crest and wave trough, caused by the slight increase in wave trough in WPB1. This kind of increase causes the change of wave force. The diffraction effects are not obvious in long-wave cases. The reflection of the wave mainly causes the wave scattering around the cylinder.

3.8. Scattered wave field around the cylinder

Fig. 22 shows the transient phase difference of wave elevation at WPB1 and WPB5 for three wavelengths with the same wave steepness (case 2, case 5 and case 8). The phase difference is the most obvious for the small wavelength case T = 7s at WPB1 and WPB5. The transient phase difference shows the anti-phase phenomenon; the value of the difference is close to 180°. For the medium wavelength case $T = 9s$, the main phase difference is about 90°; the secondary phase difference appears on the wave trough of WPB5, and the value is around 270°. For the large wavelength case $T = 15s$, the phase and amplitude of wave scatter elevation are almost the same in the front wave probe and back wave probe. Thus the phase difference is close to 0°. The wavelength has a great influence on the amplitude and phase of the front and back wave elevation of the cylinder. According to the analysis above, we can

the increase of the wave steepness, the thin and sharp wave crest shows more obvious. The weak nonlinearity presents in the wave trough because of the superposition of the incident wave and reflected wave. When the wave passes through the cylinder, the difference between the wave crest and wave trough decreases. At WPB4 and WPB5, the time history of surface elevation shows few non-linear features. As shown in Figs. 15 and 17, the wave field, which is a distance of D from the center of the cylinder, is almost the same as that around the cylinder. At the wave-facing position, the superposition of the incident wave and reflected wave decreases. Therefore, the surface elevation at WPO1 is steeper than that at WPB1. As for case 7, the surface elevation response is very close, which means the cylinder has little influence on the wave

Fig. 22. The analysis of transient phase difference between front and back wave elevation.

consider that the scattering wave field is not obvious in long wave cases; the wave diffraction is due to the wave reflection.

According to previous experimental observation on the interaction between steep waves and a single column, two types of high-frequency wave scattering can be found (Swan and Sheikh, 2015). Fig. 23 shows qualitative comparisons between experimental observation and numerical simulation of the top view of the local free surface around the cylinder. The experimental observation is referred to Swan and Sheikh (2015), and the numerical simulation condition is $T = 7$ s and $H/L = 1/10$. The wave diffraction field around the cylinder can be clearly seen. When the wave crest approaches the cylinder, the water is blocked in front of the cylinder. As the water washes back down, a disturbance radiates outwards, and concentric wave scattering (Type-1) in the upstream can be observed. Then the wave moves forward around the surface of the cylinder; the wave is divided into two parts at both sides of the cylinder, forming the edge wave, shown in Fig. 24. As the edge wave travels forward, the water moves outwards, and a pair of symmetric non-concentric wave scattering (Type-2) is developed. This may induce strong nonlinearity at the shoulders of the cylinder. When the water encounters and overlaps at the rear side of the cylinder, the run-up phenomenon can also be observed.

Fig. 24 shows comparisons between experimental observation and numerical simulation of the local free surface around the cylinder. As the wave crest passes the cylinder, the wave velocity is negative and opposite to the incident wave propagation — these waves are generally known as edge waves. Therefore, we can observe the water run-up on the back face of the cylinder. When the next wave crest approaches, the fluid closest to the cylinder's surface is driven back. These phenomena can be observed in our simulations which are displaced on the right column of Fig. 23.

Fig. 25 shows the distribution of velocity vector around the cylinder at the moment that the wave crest encounters the cylinder surface for

the wave at $T = 7$s and $H/L = 1/30, 1/16, 1/10$. For the three conditions, similar movement of water can be found. The water in front of the cylinder reaches the highest position and begins to fall under the action of gravity. The water at the rear of the cylinder begins to move upwards. For the case $T = 7$s and $H/L = 1/10$, this phenomenon is more evident than the other ones.

4. Wave interaction with two tandem cylinders

To study the wave interaction with two tandem cylinders in wave propagation, numerical simulations of different center-to-center distance S are carried out. The upstream cylinder is marked as cylinder 1, and the downstream cylinder is cylinder 2, as shown in Fig. 26. The center-to-center distances between the two cylinders are $S = 34$ m and 68 m, respectively. The total grid number is 2.87M in the numerical simulations. The computational mesh is presented in Fig. 27. In order to compare with the single-cylinder case, the same Stokes first-order wave with wave period $T = 7$ s, wave steepness $H/L = 0.1$ is adopted. The effects of tandem cylinders and the distance between the two cylinders are both discussed in this part.

Fig. 28 and Fig. 29 show the time histories of horizontal wave force with center-to-center distance $S = 34$ m and 68 m, respectively. The CPU time per wave period is about 6.44 h. For the small center-to-center distance case, the horizontal wave force of the single-cylinder is smaller than cylinder 1 and more significant than cylinder 2. This indicates that the tandem arrangement greatly influences the wave force of cylinders, and wave interaction between the cylinders is strong. For the large center-to-center distance case, the wave force of cylinder 2 almost equals that of the single-cylinder. It is an attractive appearance that when comparing the forces on the single-cylinder and the first cylinder in tandem cases, the small distance between cylinders (S) enlarges the horizontal forces but changes the phase a little; while large S-
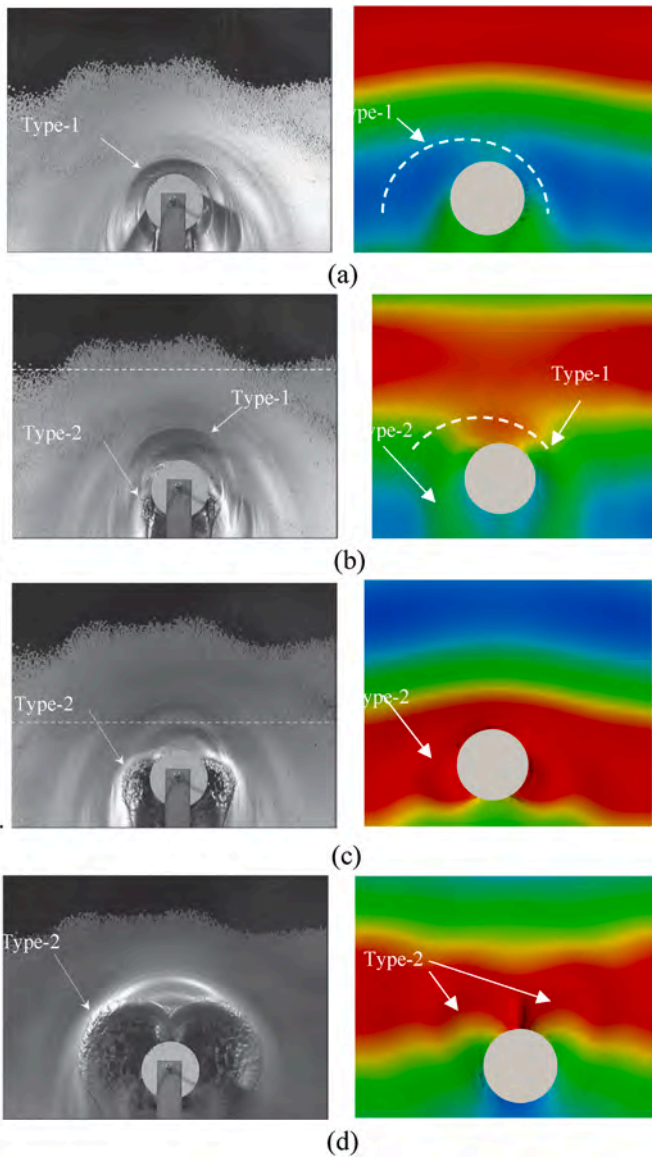
Fig. 23. Qualitative comparisons between experimental observation and numerical simulation of the local free surface around the cylinder (Top view).

Fig. 24. Qualitative comparisons between experimental observation and numerical simulation of the local free surface around the cylinder (Side view).

case also enlarges the value of the forces and shows noticeable phase difference. With the existence of the second cylinder, the front cylinder would suffer larger wave forces than the single one. This may be caused by the radiation of the front cylinder or the wave radiation of the second cylinder.

Fig. 30 and Fig. 31 show the free surface elevations in front of the cylinders with center-to-center distance $S = 34$ m and 68 m, respectively. Wave probes are placed in front of the cylinders (WPB1 and WPC1 are in front of cylinder 1 and cylinder 2, respectively) and at the middle point between the cylinders (WP0). It can be seen that the crest height is increased in front of cylinder 1 and cylinder 2 in both cases due to the wave run-up on the cylinders. The surface elevation on the first cylinder is almost the same in cases $S = 34$m and 68m, but the forces on them are totally different, as shown in Figs. 28 and 29. It means there

exists dynamic non-linear wave force.

The crest height in front of the cylinders is about 2.1 times the incident wave amplitude. The relative crest height A/A_0 in front of cylinders is similar for each case, but the waveform of cylinder 1 and cylinder 2 shows a significant difference for $S = 34$ m and 68 m. For the larger center-to-center distance case, the waveform of cylinder1 and cylinder 2 is similar at crest and trough. For the smaller center-to-center distance case, the waveform around cylinder 1 is symmetrical, while the waveform around cylinder 2 shows asymmetrical characters with shallow troughs and sharp crests. At the middle point of the cylinders, the relative crest height of the two cases shows a significant difference. The crest height for the $S = 34$ m case is about two times the incident wave amplitude, while for the $S = 68$ m case, it almost equals incident wave amplitude. This indicates that when the cylinders are close to each other, the wave interaction between the cylinders can be relatively
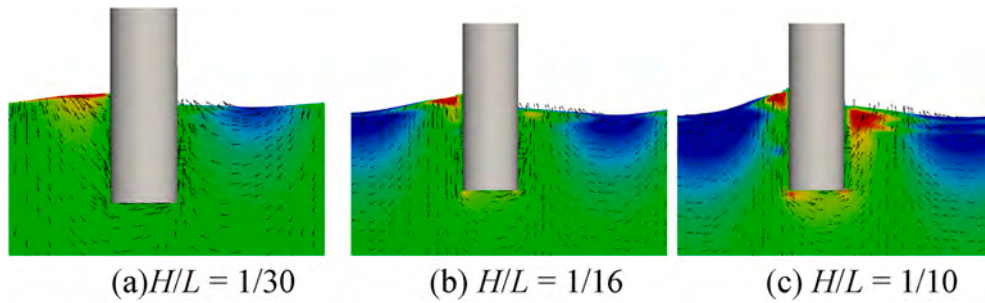
Fig. 25. Distribution of velocity vector around the cylinder.
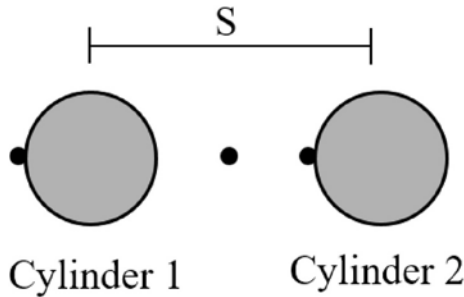
Fig. 26. Arrangement of the two tandem cylinders.

strong. In the meantime, it can be observed that in $S = 68$m, the curve of wave elevation in the middle point has a non-linear effect. These large order wave forces may be the reason that causes the phase difference in Fig. 29.

In order to investigate the wave field around the two tandem cylinders, the surface elevation in the numerical wave tank is studied. Fig. 32 and Fig. 33 show the local free surface around the tandem cylinders for $S = 34$ m and 68 m. The wave diffraction patterns around the cylinders can be seen for both cases. When the wave crest approaches cylinder 1, the water is blocked in front of the cylinder, and a concentric wavefield can be observed. As shown in Fig. 32(a), two waveforms can be found around cylinder 1 due to wave diffraction. This is specified by Swan and Sheikh (2015). As water travels about half of cylinder 1, the free surface elevation decreases, shown in Fig. 32(b), and the non-concentric wavefield can be found. Fig. 32(c) shows the increase in surface elevation as the wave travels in front of cylinder 2, and two semi-circular waves can be seen. This is because the incident and reflected waves meet behind cylinder 1 and interfere with each other. Fig. 32(d) shows the decrease when the wave travels over cylinder 2. A similar phenomenon can be found in Fig. 33. However, the wave interaction between the two tandem cylinders is not obvious due to the larger center-to-center distance. We consider these as a near-trapping-like phenomenon. The near-trapping phenomenon happens in the four-cylinder arrangement, the water between the four cylinders is trapped inside them, and the wave elevation is significantly large. The
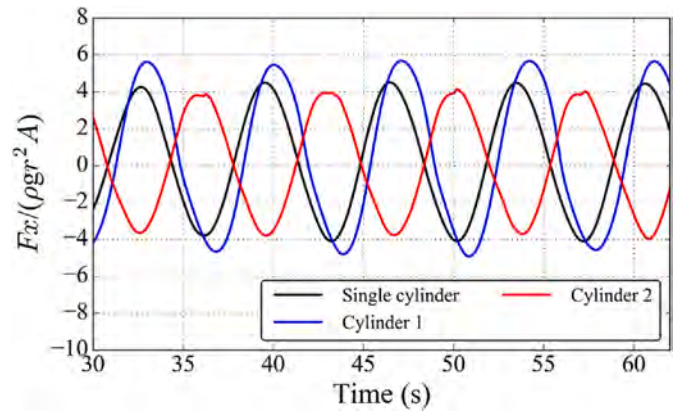
Fig. 28. Time series of horizontal wave force with center-to-center distance S = 34m.
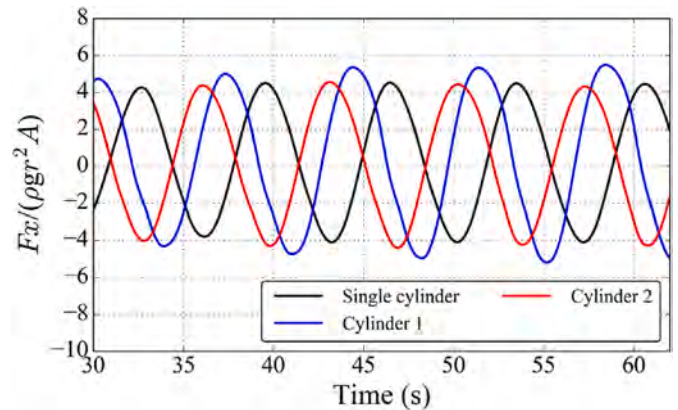
Fig. 29. Time series of horizontal wave force with center-to-center distance S = 68m.
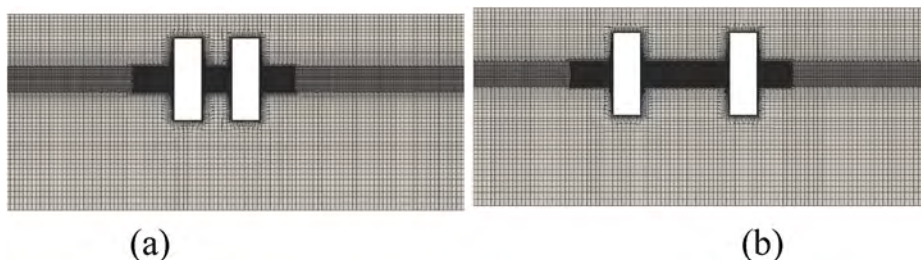
Fig. 27. Computational mesh: (a) S = 34 m (b) S = 68 m.
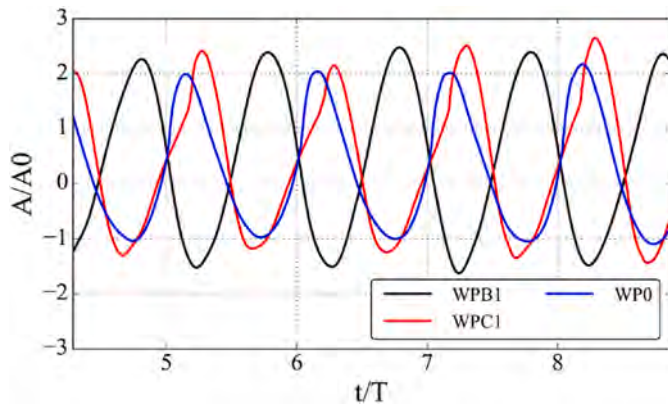
Fig. 30. Free surface elevations in front of the cylinders with center-to-center distance S = 34m.
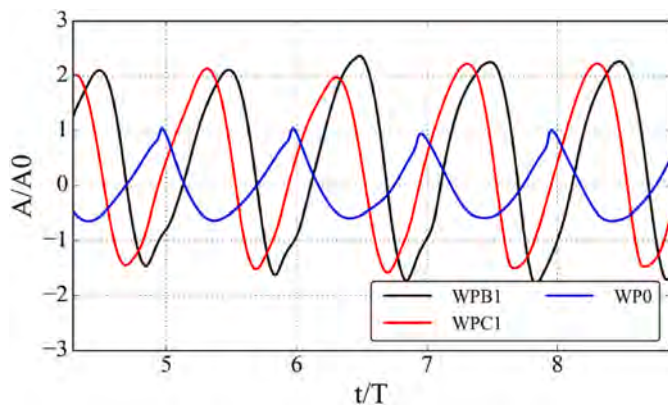
Fig. 31. Free surface elevations in front of the cylinders with center-to-center distance S = 68m.

wavefield between the two cylinders shows a trapping phenomenon in Fig. 32, and the wave elevation in the field is also significantly high.

5. Conclusions

In the present work, numerical simulations of wave run-up on a fixed surface-piercing cylinder in regular waves as well as tandem cylinders with different distances are performed by the in-house naoe-FOAM-SJTU solver. The primary studies are listed below:

The influence of wave steepness is discussed on a single cylinder. Three wave heights ($H/L = 1/30$, $1/16$, $1/10$) and three wavelengths ($T = 7s$, $9s$, $15s$) are conducted to investigate the wave run-up phenomenon. The predicted RAOs of local surface elevation are compared with the experimental data, and good agreement can be acquired. The surface elevation around the cylinder and the dynamic pressure increases with the increasing wave height. In short wave cases, the cylinder has more influence on waves, and in long waves with small wave steepness cases, the cylinder shows minor effects on waves. At the strong non-linear interaction location, the secondary crests can be observed for steeper waves. This could be caused by the overlap between the backward wave from the rear part and the incident wave. The present CFD solver could capture concentric and non-concentric wave fields around the cylinder. For the highest steepness wave, the run-up on the side of the cylinder shows non-linear characteristics. For the interaction between waves and tandem cylinders, we found that with the increase of the KC number, the wave run-up on the front of the cylinder decreases, and the wave depresses on the rear of the cylinder decreases. With the existence of the back cylinder, the horizontal forces and surface elevation on the front cylinders become larger compared to the single cylinder. When the front cylinder affects the back cylinder, there shows a likely near-trapping phenomenon, which shows large wave elevation between two cylinders. As the center-to-center distance increases, the large phase difference in force is shown between the single-cylinder and the front cylinder. In the future, it needs to be figured out whether the radiation of the front cylinder or that of the back cylinder enlarges these values.
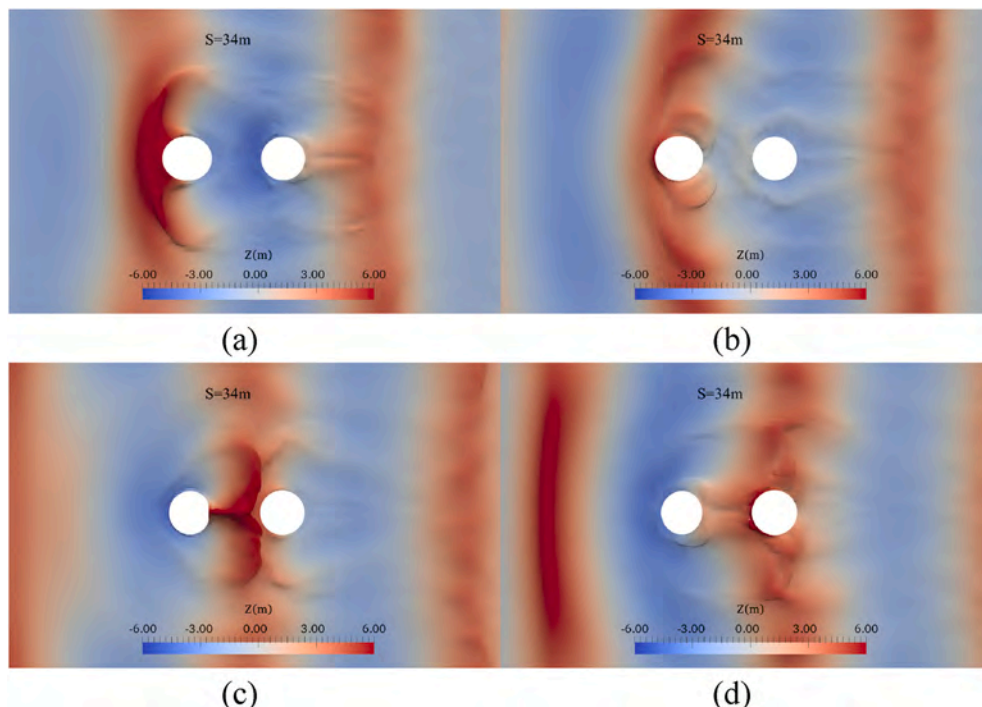
Fig. 32. Free surface elevations around the cylinders with center-to-center distance S = 34m: (a) t/T = 10, (b) t/T = 10.21, (c) t/T = 10.42, (d) t/T = 10.86.
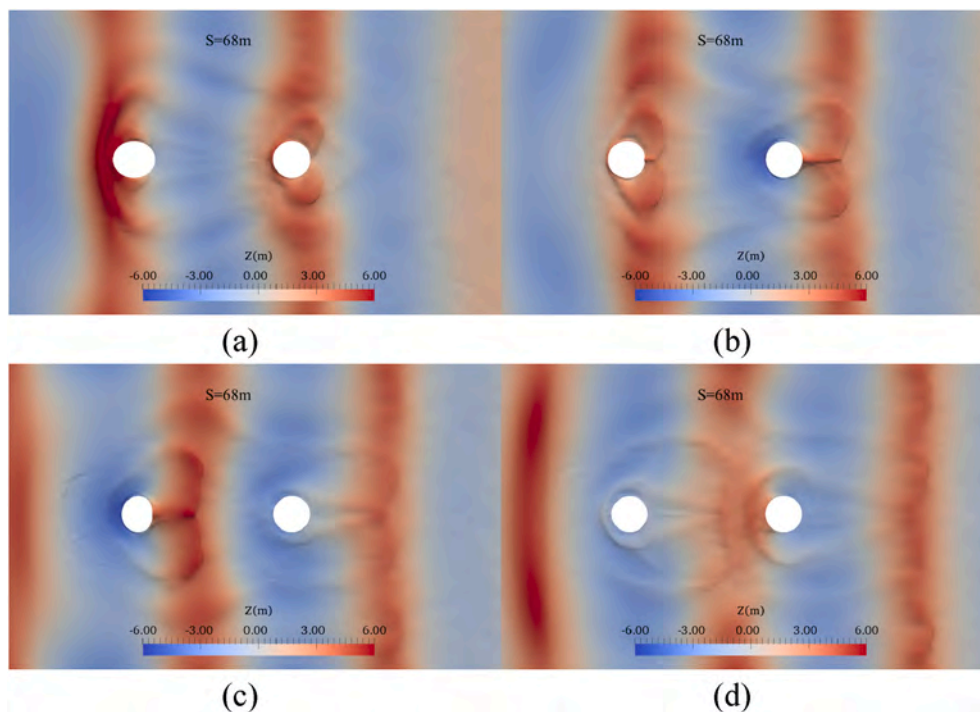
Fig. 33. Free surface elevations around the cylinders with center-to-center distance S = 68m: (a) t/T = 10, (b) t/T = 10.21, (c) t/T = 10.42, (d) t/T = 10.86.

CRediT authorship contribution statement

Zhenghao Liu: Data curation, Writing – original draft, preparation, Visualization, Investigation, Software, Validation. **Weiwen Zhao:** Software, Data curation, Visualization, Investigation, Validation. **Decheng Wan:** Supervision, Conceptualization, Methodology, Investigation, Writing – review & editing.

Declaration of competing interest

The authors declare the following financial interests/personal relationships which may be considered as potential competing interests:

Acknowledgments

References

Cao, D., Huang, Z., He, F., Jian, W., Lo, E.Y.M., 2017. An improved prediction for wave runup on a circular cylinder. Coast Eng 59, 1750013.
Cao, H.J., Wan, D.C., 2014. Development of multidirectional non-linear numerical wave tank by naoe-FOAM-SJTU solver. Int. J. Ocean Syst. Eng. 4, 52–59.
Cao, H.J., Wan, D.C., 2015. RANS-VOF solver for solitary wave run-up on a circular cylinder. China Ocean Eng. 29, 183–196.
Cao, H.J., Wan, D.C., 2017. Benchmark computations of wave run-up on single cylinder and four cylinders by naoe-FOAM-SJTU solver. Appl. Ocean Res. 65, 327–337.
Chakrabarti, S.K., Tam, W.A., 1975. Wave height distribution around a vertical cylinder. J. Waterway Div. 101, 225–230.
Chen, L.F., Zang, J., Hillis, A.J., Morgan, G.C.J., Plummer, A.R., 2014. Numerical investigation of wave-structure interaction using OpenFOAM. Ocean Eng 88, 91–109.
Contento, G., Francescutto, A., Lalli, F., 1998. Non-linear wave loads on single vertical cylinders: pressure and wave field measurements and theoretical predictions. The 8th International Offshore and Polar Engineering Conference, pp. 526–534.
Contento, G., D'este, F., Sicchiero, M., Codiglia, R., Calza, M., 2004. Run-up and wave forces on an array of vertical circular cylinders: experimental study on the second order near trapping. The 14th International Offshore and Polar Engineering Conference, pp. 402–409.

Corvaro, S., Crivellini, A., Marini, F., Cimarelli, A., Capitanelli, L., Mancinelli, A., 2019. Experimental and numerical analysis of the hydrodynamics around a vertical cylinder in waves. J. Mar. Sci. Eng. 7, 453.
Danmeier, D.G., Seah, R.K., Finnigan, T., Roddier, D., Aubault, A., Vache, M., Imamura, J.T., 2008. Validation of wave run-up calculation methods for a gravity based structure. The 27th International Conference on Offshore Mechanics and Arctic Engineering, pp. OMAE2008–57625.
Galvin, C.J., Hallermeier, R.J., 1972. Wave runup on vertical cylinders. Coast. Eng. 1, 1955–1974.
Greenshields, C.J., 2018. OpenFOAM User Guide Version 6. The OpenFOAM Foundation.
Gentaz, L., Luquet, R., Alessandrini, B., Ferrant, P., 2004. Numerical simulation of the 3D viscous flow around a vertical cylinder in non-linear waves using an explicit incident wave model. The 23rd International Conference on Offshore Mechanics and Arctic Engineering, pp. 157–163.
Hajivand, A., Mousavizadegan, S.H., 2015. Virtual maneuvering test in CFD media in presence of free surface. Int. J. Nav. Arch. Ocean Eng. 7, 540–558.
Havelock, T.H., 1940. The pressure of water waves upon a fixed obstacle. Proc. R. Soc. London, Ser. A. 175, 409–421.
Hirt, C.W., Nichols, B.D., 1981. Volume of fluid (VOF) method for the dynamics of free boundaries. J. Comput. Phys. 39, 201–225.
Hu, Z.Z., Greaves, D., Raby, A., 2016. Numerical wave tank study of extreme waves and wave-structure interaction using OpenFoam®. Ocean Eng 126, 329–342.
Kriebel, D.L., 1992. Non-linear wave interaction with a vertical circular cylinder. Part II: wave run-up. Ocean Eng 19 (1), 75–99.
Kristiansen, T., Baarholm, R., Stansberg, C.T., 2004. Validation of second-order analysis in predicting diffracted wave elevation around a vertical circular cylinder. The 14th International Offshore and Polar Engineering Conference, pp. 342–349.
Lee, K.H., Kim, D.S., Kim, C.H., Lee, S.K., Kee, S.T., 2007. Wave run-up on vertical cylinder by 3-dimensional VOF method. The 8th International Offshore and Polar Engineering Conference, pp. 2679–2683.
Lin, Y.H., Chen, J.F., Lu, P.Y., 2017. A CFD model for simulating wave run-ups and wave loads in case of different wind turbine foundations influenced by non-linear waves. Ocean Eng 129, 428–440.
Martin, A.J., Easson, W.J., Bruce, T., 2001. Runup on columns in steep, deep water regular waves. J. Waterw. Port. Coast. 127 (1), 26–32.
Matsumoto, F.T., Watai, R.A., Simos, A.N., Ferreira, M.D.A.S., 2013. Wave run-up and air gap prediction for a large-volume semi-submersible platform. J. Offshore Mech. Arct. Eng. 135, 011302.
Mohseni, M., Esperanca, P.T., Sphaier, S.H., 2018. Numerical study of wave run-up on a fixed and vertical surface-piercing cylinder subjected to regular, non-breaking waves using OpenFOAM. Appl. Ocean Res. 79, 228–252.
Morris-Thomas, M.T., Thiagarajan, K., Krokstad, J.R., 2002. An experimental investigation of wave steepness and cylinder slenderness effects on wave run-up. The 21st International Conference on Offshore Mechanics and Arctic Engineering, pp. OMAE2002–28050.
Morris-Thomas, M.T., Thiagarajan, k., 2004. The run-up on a cylinder in progressive surface gravity waves: harmonic components. Appl. Ocean Res. 26, 98–113.
Nam, B.W., Hong, S.Y., Sung, H.G., 2012. Numerical simulation of diffracted wave by vertical cylinder using VOF method. Int. J. Offshore Polar. 22 (1), 7–12.

Nielsen, F.G., 2003. Comparative study on airgap under floating platforms and run-up along platform columns. Mar. Struct. 16, 97–134.

Ramirez, J., Frigaard, P., Andersen, T.L., de Vos, L., 2013. Large scale model test investigation on wave run-up in irregular waves at slender piles. Coast. Eng. 72, 69–79.

Roache, P.J., 1994. Perspective: a method for uniform reporting of grid refinement studies. J Fluids Eng 116, 405–413.

Sanada, M., 1998. A Study of Second-Approximation Analysis Results and Application for Non-linear Diffraction Wave According to Large Coastal Structure. Doctoral dissertation. Nagoya University, p. 223p.

Shan, T.B., Yang, J.M., Li, X., Xiao, L.F., 2011. Experimental investigation on wave run-up characteristics along columns and air gap response of semi-submersible platform. J. Hydrodyn. 23, 625–636.

Shen, Z.R., Wan, D.C., Carrica, P.M., 2015. Dynamic overset grids in OpenFOAM with application to KCS self-propulsion and maneuvering. Ocean Eng 108, 287–306.

Shen, Z.R., Wan, D.C., 2016. An irregular wave generating approach based on naoe-FOAM-SJTU solver. China Ocean Eng. 30, 177–192.

Sun, L., Zang, J., Chen, L., Taylor, R.E., Taylor, P.H., 2016. Regular waves onto a truncated circular column: a comparison of experiments and simulations. Appl. Ocean Res. 59, 650–662.

Stern, F., Wilson, R., Shao, J., 2006. Quantitative V&V of CFD simulations and certification of CFD codes. Int. J. Numer. Methods Fluid. 50 (11), 1335–1355.

Swan, C., Sheikh, R., 2015. The interaction between steep waves and a surface-piercing column. Philos. Trans. R. Soc. London, Ser. A 373, 20140114.

Teigen, P., Niedzwecki, J.M., 2003. Wave diffraction effects and runup around multicolumn structure. The 8th International Offshore and Polar Engineering Conference, pp. 137–144.

Trulsen, K., Teigen, P., 2002. Wave scattering around a vertical cylinder: fully non-linear potential flow calculations compared with low order perturbation results and experiment. The 21st International Conference on Offshore Mechanics and Arctic Engineering. OMAE2002-28173.

Wang, J.H., Wan, D.C., 2016. Numerical simulation of pure yaw motion using dynamic overset grid technology. Chinese J. Hydrodyn. 31, 567–574.

Wang, J., Zhao, W., Wan, D., 2019. Development of naoe-FOAM-SJTU solver based on OpenFOAM for marine hydrodynamics. J. Hydrodyn. 31, 1–20.

Weller, H.G., Tabor, G., Jasak, H., Fureby, C., 1998. A tensorial approach to computational continuum mechanics using object oriented techniques. Comput. Phys. 12, 620–631.

Yang, I.-J., Lee, Y.-G., Jeong, K.-L., 2015. Numerical simulation of the free surface around a circular column in regular waves using modified marker-density method. Int. J. Nav. Arch. Ocean 7, 610–625.

Ye, H.X., Wan, D.C., 2017. Benchmark computations for flows around a stationary cylinder with high Reynolds numbers by RANS-overset grid approach. Appl. Ocean Res. 65, 315–326.

Yoon, S.-H., Kim, D.-H., Sadat-Hosseini, H., Yang, J., Stern, F., 2016. High-fidelity CFD simulation of wave run-up for single/multiple surface-piercing cylinders in regular head waves. Appl. Ocean Res. 59, 687–708.